

Analysis and Design of a Millimeter-Wave Cavity-Backed Circularly Polarized Radiator Based on Fundamental Theory of Multi-Port Oscillators

Peyman Nazari^{ID}, Student Member, IEEE, Saman Jafarloo, Student Member, IEEE, and Payam Heydari, Fellow, IEEE

Abstract—This paper presents the design and implementation of a millimeter-wave fundamental frequency circularly polarized radiator, which employs a multi-port cavity as the core of a high-*Q* resonator, a power combiner, and an antenna. A general theory of multi-port oscillators—and in particular, the widely used circularly symmetric oscillator topologies—is presented, which quantitatively investigates and predicts all possible oscillation states, their associated modes of operation, and the oscillation stability. The outcomes of this theory are utilized to design a power-optimized eight-port rotationally symmetric radiator, excited at the oscillation state with a 45 phase difference between the adjacent ports, which, in turn, enables a high-efficiency circularly polarized radiation. Fabricated in 0.13- μm BiCMOS process, this cavity-backed circularly polarized radiator operates at the frequency of 114 GHz and achieves 14.2-dBm equivalent-isotropic-radiated power (EIRP), 5.2% dc-to-EIRP conversion efficiency, 8.2 dBm radiated power, 1.3% dc-to-radiation efficiency, and -99.3 dBc/Hz phase noise at 1-MHz offset, without using silicon lens.

Index Terms—Cavity, circular polarization, millimeter-wave (mm-wave), multi-port, multi-port oscillator, radiator, ring oscillator, silicon, theory.

I. INTRODUCTION AND MOTIVATION

OPERATION in millimeter-wave (mm-wave) and THz bands (e.g., 30–3000 GHz) has re-gained enormous attention due to emerging applications, such as 10-Gbit wireless communications [1]–[3], high-resolution passive/active imaging, and radar sensing [4]–[6]. All these applications mandate high-power and high-efficiency signal generation and radiation. On the other hand, the limited power available from active devices together with the excessive loss of passives at such high frequencies makes the design of high-power signal generators and radiators extremely challenging [7], [8]. Recently, a number of circuit architectures for mm-wave signal power generation have been introduced [9]–[11], which

Manuscript received May 2, 2017; revised August 10, 2017; accepted September 4, 2017. Date of publication October 25, 2017; date of current version November 21, 2017. This paper was approved by Guest Editor Chih-Ming Hung. This work was supported in part by the *(SAIT)'s Global Research Outreach Program, in part by NSF under Award ECCS 1408547 and Award ECCS 1611575, and in part by the Samsung Advanced Institute of Technology (SAIT). (Corresponding author: Peyman Nazari.)

P. Nazari was with the Department of Electrical Engineering and Computer Science, University of California at Irvine, Irvine, CA 92697, USA. He is now with Qualcomm Inc. San Diego, CA 92121 USA (e-mail: pnazari@uci.edu).

S. Jafarloo and P. Heydari are with the Department of Electrical Engineering and Computer Science, University of California at Irvine, Irvine, CA 92697, USA.

Color versions of one or more of the figures in this paper are available online at <http://ieeexplore.ieee.org>.

Digital Object Identifier 10.1109/JSSC.2017.2753823

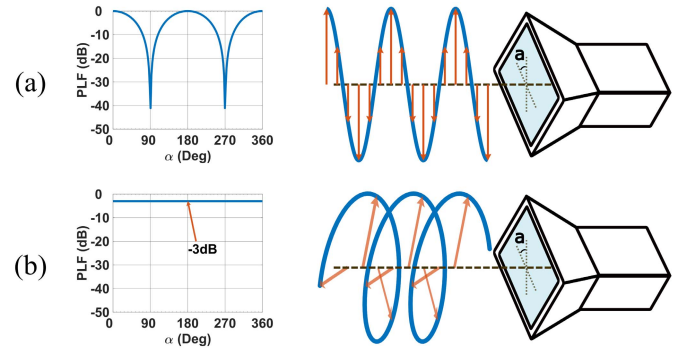


Fig. 1. Rotation of the RX antenna around its normal axis and its impact on polarization loss factor when receiving (a) linearly polarized and (b) circularly polarized EM wave.

incorporate novel oscillator and on-chip power-combining topologies. To further boost the radiated output power and equivalent-isotropic-radiated power (EIRP), [3], [5], and [12] expand these topologies to on-chip array configurations with linearly polarized radiation.

To increase the signal-to-noise ratio in a line-of-sight wireless communication, the radiation polarization of the TX and the RX antennas must match for maximum detection gain. For linearly polarized antennas, this requires the accurate alignment of the TX and RX antennas [13], [14]. Otherwise, the RX antenna cannot efficiently receive the TX signal to the extent that the detection gain significantly drops when the polarization of the TX and RX antennas are orthogonal [Fig. 1(a)]. Furthermore, for many applications, the transmitted electromagnetic (EM) wave is subject to random polarization shifts, for example, due to scattering after reflection from rough surfaces or propagation through an ionized medium, which is likely to happen in tissue imaging [13]. On the other hand, circularly polarized waves are resilient to such polarization shifts and misalignments, as shown in Fig. 1(b). References [15]–[20] demonstrated integrated systems for generation and radiation of circularly polarized mm-wave signals. Furthermore, [14] and [21] proposed solutions to control the polarization of the radiated waves. However, a design approach to co-design a high-power, low-phase-noise oscillator and a circularly polarized radiator seems vital so as to achieve high radiated power and dc-to-EIRP conversion efficiency.

This paper introduces a high-power/efficiency multi-port oscillator/radiator, which employs a monolithic multi-port cavity-based structure that concurrently performs as a resonator, a power combiner, and an antenna so as to avoid

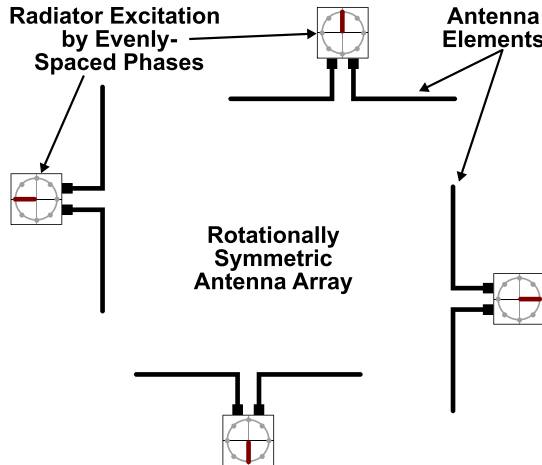


Fig. 2. Generation of circularly polarized radiation using four linearly polarized antennas excited by evenly spaced phases.

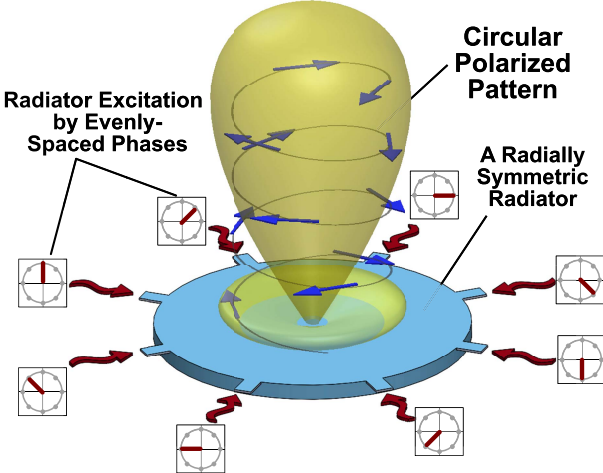


Fig. 3. Generation of circularly polarized radiation using a multi-port rotationally symmetric radiator excited by evenly spaced phases.

the extra use of lossy coupling and power-combining passive networks or power-hungry amplifiers. Moreover, this structure enables circularly polarized radiation by exciting a multi-port rotationally symmetric radiator with distinct evenly spaced phases of an RF signal. To design this oscillator, theoretical foundations to analyze oscillation states, operation modes, and oscillation stability in a generic multi-port oscillator and a widely used subset, namely, the circularly symmetric oscillators, are introduced. The outcomes of this theory are utilized to design this multi-port oscillator/radiator for high-power/efficiency oscillation and circularly polarized radiation.

A. Generation of Circularly Polarized Radiation

One method to generate circularly polarized radiation is to feed multiple distinct antenna elements of a circular array with multiple excitation sources and set the excitation phases to be distinct and evenly spaced [22]. As a result, proper radiative currents satisfying the conditions for circularly polarized radiation are formed, as shown in Fig. 2 [23]. Alternatively, if a rotationally symmetric antenna is excited by distinct evenly spaced phases of an RF signal (i.e., the total phase rotation of $1 \times 360^\circ$), the resultant radiation is circularly polarized, as shown in Fig. 3. References [15] and [16] used multiple cross-coupled pairs as standalone negative

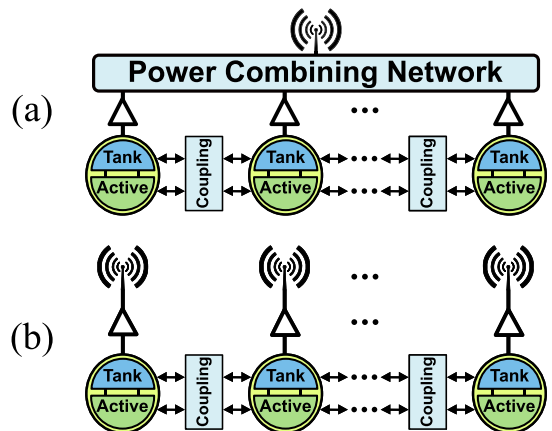


Fig. 4. (a) On-chip and (b) spatial power combination methods.

resistances to excite a ring- or a slot-ring-shaped radiator with distinct evenly spaced phases. However, high-power oscillation at near- f_{\max} frequencies necessitates the use of optimal topologies for the negative-resistance cells [7], [8]. Furthermore, reliable radiation mandates oscillator structures with a single and well-defined oscillation state, where auxiliary phase-locking or injection-locking circuitry is often required. References [14] and [20] incorporated antenna buffers to force the desired signal phase at different ports of the radiator, thereby controlling the radiation polarization. Nonetheless, the use of power-hungry mm-wave antenna buffers degrades the overall dc-to-EIRP conversion efficiency. This calls for a multi-port radiator that can maximally extract the RF power from the active devices while providing proper excitation phases for circularly polarized radiation.

B. Power Generation and Combining Methods

Various oscillator topologies have been examined to provide the optimum voltage-gain condition for maximum power generation [7], [8], [24], [25]. While these approaches are able to extract the maximum RF power from a single active device at the frequency of interest, this output power is still far too low to be considered for mm-wave radiators. To further boost the output power level, power-combining schemes are employed to combine the RF output powers of multiple oscillators. Primarily, this has been achieved by employing either an on-chip power-combining network [9], [11] [Fig. 4(a)] or multiple antenna elements for constructive power combining in free space [3], [7], [12], [26], [27] [Fig. 4(b)]. In both methods, in addition to the power-combining network, a coupling network is employed to ensure phase-locked oscillation of all constituent oscillator elements. As will be explained in Sections III and IV, the multi-port cavity introduced in this paper combines the oscillation signals injected from its different ports and directly radiates the combined signal into the free space. The same structure also acts as a shared resonance tank (Fig. 5). Therefore, the coupling networks and the antenna buffers are avoided, thereby achieving high-power and dc-to-EIRP conversion efficiency.

II. ANALYSIS OF MULTI-PORT OSCILLATORS

It is desirable to explore a multi-port oscillator circuit with multiple active devices exciting a multi-port passive structure,

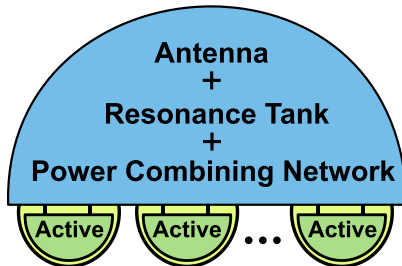


Fig. 5. Proposed mm-wave concurrent oscillation, power combining, and radiation scheme.

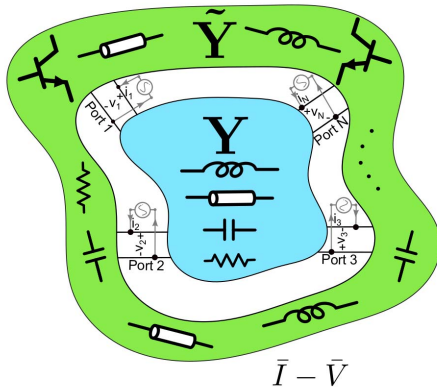


Fig. 6. Generic multi-port oscillator comprised of an N -port passive and an N -port excitation network.

as a shared resonator, so as to produce much higher oscillation power and efficiency than current oscillators. However, the use of multiple independent elements to excite a multi-port passive structure can lead to multiple stable oscillation states [28]–[30]. Inherent to such systems, this attribute calls for a careful study that can quantitatively discover oscillation conditions that result in different oscillation states within a multi-port structure consisting of multiple active devices and passive networks.

Consider an N -port passive structure, which is represented by its Y -parameters matrix \mathbf{Y} . Based on the Nyquist stability theorem, an N -port excitation network with right-half-plane poles, comprising active and passive components, exists, which can potentially generate oscillation if being connected to this passive network. This excitation network is described by its admittance matrix $\tilde{\mathbf{Y}}$, as shown in Fig. 6.

To assess the oscillation condition, we construct the total admittance matrix \mathbf{Y}_t , ($\mathbf{Y}_t \bar{V} = \bar{I}$), defined as $\mathbf{Y}_t = \mathbf{Y} + \tilde{\mathbf{Y}}$. As a necessary condition, a circuit will autonomously oscillate if a non-zero port voltage exists for a zero-port current [31]. Thus, the total admittance matrix must have a determinant of zero for sustainable oscillation, that is

$$\det(\mathbf{Y}_t(j\omega)) = \det(\mathbf{Y}(j\omega) + \tilde{\mathbf{Y}}(j\omega)) = 0. \quad (1)$$

Any linear system is characterized by a set of eigenvectors \bar{U}_m (for $1 \leq m \leq N$), which determine its basis functions. Upon exciting the system with its m th eigenvector, the system response is identical to its input except for a multiplicative constant commonly known as its m th eigenvalue $\lambda_{t,m}$, and the system is said to operate in its mode- m . Furthermore,

$\det(\mathbf{Y}_t(j\omega)) = \prod_{m=1}^N \lambda_{t,m}(j\omega)$. Therefore, (1) becomes

$$\prod_{m=1}^N \lambda_{t,m}(j\omega) = 0. \quad (2)$$

Equation (2) can hold at several distinct frequencies. Oscillation at a frequency of ω_{osc} requires, at least, one zero eigenvalue at this frequency, i.e., $\lambda_{t,k}(j\omega_{\text{osc}}) = 0$.

Definition 1 (Oscillation State): In an N -port oscillator characterized by its total admittance matrix \mathbf{Y}_t , any $\omega_i \in \mathbb{R}^+$ and $\lambda_{t,m}$ (for $1 \leq m \leq N$) satisfying $\lambda_{t,m}(j\omega_i) = 0$ defines a distinct oscillation state.

The stability of an oscillation state, i.e., the resilience of its amplitude and phase against any perturbation, is governed by the nonlinear dynamics of the system [31], [32]. The nonlinearity is contributed by the nonlinear active components utilized in the excitation network. More specifically, $\tilde{\mathbf{Y}} = \tilde{\mathbf{Y}}(j\omega, \bar{V})$, and therefore, $\lambda_{t,m}(j\omega) = \lambda_{t,m}(j\omega, \bar{V})$. Hence, solving (2) also determines the amplitude of oscillation [31], [33]. The stability of oscillation will be discussed quantitatively in Section V. Intuitively speaking, if the response of the excitation network to a disturbance vector is in the opposite direction of this disturbance, the nonlinearity would counteract the perturbation, and thus, the stable oscillation will be acquired.

Definition 2 (Mode- m Input Admittance $Y_{\text{in},m}$): The driving-point input admittance vector of an N -port network operating in its mode- m (i.e., excited by \bar{U}_m), $\bar{Y}_{\text{in},m}$, is expressed as

$$\bar{Y}_{\text{in},m} = \bar{I}_m \oslash \bar{U}_m = (\mathbf{Y}_t \bar{U}_m) \oslash \bar{U}_m \quad (3)$$

where \oslash denotes the elementwise division operator. Equation (3) is readily simplified to

$$\bar{Y}_{\text{in},m} = (\lambda_{t,m} \bar{U}_m) \oslash \bar{U}_m = (\lambda_{t,m}, \dots, \lambda_{t,m})^T. \quad (4)$$

Equation (4) reveals that the input admittance of all ports are equal to $\lambda_{t,m}$ when the network is excited by \bar{U}_m

$$Y_{\text{in},m}(j\omega) = \lambda_{t,m}(j\omega). \quad (5)$$

$Y_{\text{in},m}$ is called mode- m input admittance.

Consequently, $\lambda_{t,m} = 0$ provides the necessary condition for oscillation, which requires “seeing” an open circuit looking into each port. If $\text{Re}\{\lambda_{t,m}\} < 0$, while $\text{Im}\{\lambda_{t,m}\} = 0$, the structure can generate oscillation with growing amplitude, until the nonlinearity of the active devices limits its growth. This is justified by noting that a purely resistive lossy component $1/G_L = -1/\text{Re}\{\lambda_{t,m}\}$ can be connected to each port and the structure can still oscillate, since the resultant port input admittance is zero ($\lambda_{t,m} + G_L = 0$). Thus, for any lower amount of loss ($G_L < -\text{Re}\{\lambda_{t,m}\}$), the response can potentially grow.

Definition 3 (Single-State Oscillator): If $\lambda_{t,m}(j\omega_i) = 0$ for one and only one ω_i and $\lambda_{t,m}$, the oscillator is said to be a single-state oscillator.

Since $\mathbf{Y}_t(j\omega_0) \bar{U}_m = \lambda_{t,m}(j\omega_0) \bar{U}_m = 0$, we conclude that for a sustainable single-state oscillation, the port voltage vector, \bar{V} , is always proportional to its eigenvector, i.e., $\bar{V} \propto \bar{U}_m$. On the other hand, if multiple oscillation states exist, each port voltage is a linear combination of the eigenvectors associated

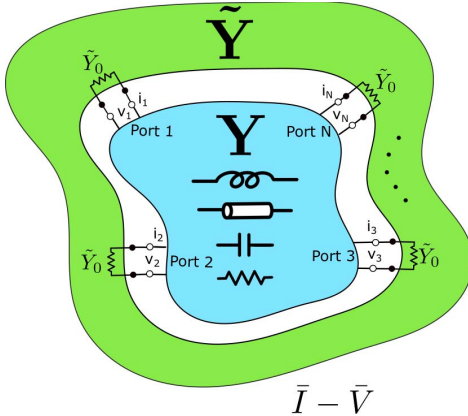


Fig. 7. N -port passive network terminated with identical negative admittances, \tilde{Y}_0 .

with the modes of those states. Note that the frequency of the oscillation states is not necessarily the same, and thus, the superposition is only valid in the time domain and not in the phasor domain.

Diagonalization of \mathbf{Y} leads to $\mathbf{Y} = \mathbf{U}\Lambda\mathbf{U}^{-1}$, where $\Lambda = \text{diag}(\lambda_1, \dots, \lambda_N)$ is diagonal matrix of eigenvalues and the columns of \mathbf{U} are the corresponding eigenvectors. Therefore, (1) is written as

$$\det(\mathbf{Y}_t) = \det(\mathbf{U}\Lambda\mathbf{U}^{-1} + \tilde{\mathbf{Y}}) \quad (6)$$

$$= \det(\Lambda + \mathbf{U}^{-1}\tilde{\mathbf{Y}}\mathbf{U}) = 0. \quad (7)$$

Given a passive network with Y-parameters matrix of \mathbf{Y} , (6) or (7) can be satisfied by many choices for $\tilde{\mathbf{Y}}$. The choice of one network over another often involves considering other design factors, including power efficiency, multi-state uncertainty issue and suppression of unwanted oscillation states, chip area, and phase noise. In addition, in many practical cases, some form of symmetry exists in either the passive or the excitation, or both networks. The notion of symmetry, besides ease of implementation, is found to be advantageous in controlling the oscillation states and mitigating multi-state problem. In the following, we build an analytical foundation for rotationally symmetric oscillators, which covers a broad range of oscillator topologies, including the proposed multi-port circular-cavity-based oscillator.

A. Excitation by N Identical Single-Port Elements

This scenario occurs by connecting identical single-port excitation elements, each with an admittance of \tilde{Y}_0 , to all ports of the passive network, as shown in Fig. 7. Therefore, we have $\tilde{\mathbf{Y}} = \tilde{Y}_0\mathbf{I}$. By substituting this expression in (7), the equation $\det(\Lambda + \tilde{Y}_0\mathbf{I}) = 0$ is derived. The determinant becomes zero only if \tilde{Y}_0 is equal to negative of one of the eigenvalues of \mathbf{Y} . In other words,

$$\tilde{Y}_0(j\omega_{\text{osc}}) = -\lambda_m(j\omega_{\text{osc}}) \quad (8)$$

then an oscillation state at ω_{osc} exists in mode- m . The single-cavity multiple-device oscillator in [28] is an example of this case for which $\tilde{Y}_0 = -\lambda_0$ at ω_{osc} , while $\tilde{Y}_0(j\omega) + \lambda_i(j\omega) > 0$ for $\forall i \neq 0$. Therefore, oscillation states in other modes are suppressed.

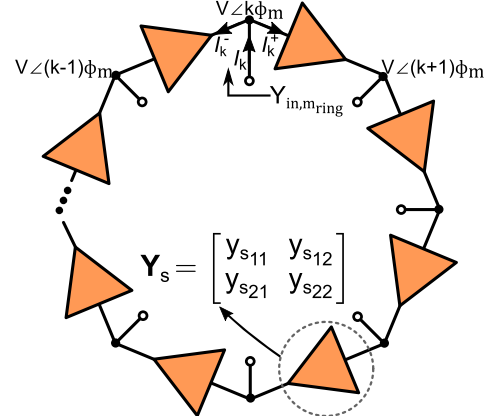


Fig. 8. Driving-point input admittance of an N -stage ring oscillator.

B. Symmetric Circuits—Circulant Admittance Matrix

In this section, the oscillation condition for circuits with rotational symmetry is analyzed. In such circuits, if the port numbers are shifted (clockwise or counterclockwise), the network parameters (elements of the corresponding Y-matrix) remain the same. Rotational symmetry is found in many topologies, such as ring- or star-shaped symmetric oscillators [34]. For rotationally symmetric topologies, the total admittance matrix is in the form of a symmetric circulant matrix, as denoted in the following equation:

$$\mathbf{Y}_t = \begin{bmatrix} y_{t11} & y_{t12} & \cdots & y_{t1N} \\ y_{t1N} & y_{t11} & \cdots & y_{t1N-1} \\ \vdots & \ddots & \ddots & \vdots \\ y_{t12} & y_{t13} & \cdots & y_{t11} \end{bmatrix} \triangleq \text{circ}(y_{t11}, y_{t12}, \dots, y_{t1N}). \quad (9)$$

As it is true for any circulant matrix, the elements of eigenvectors of \mathbf{Y}_t are Fourier basis functions covering the entire space, that is

$$\overline{U}_m = (1, e^{j\phi_m}, e^{j2\phi_m}, \dots, e^{j(N-1)\phi_m})^T \quad (10)$$

where $\phi_m = 2\pi m/N$. In addition, the eigenvalues are directly derived as a linear combination of these Fourier basis functions with Y-parameters denoting its coefficients, that is

$$\begin{aligned} \lambda_{t,m} &= y_{t11} + y_{t12}e^{j\phi_m} + \cdots + y_{t1N}e^{j(N-1)\phi_m} \\ &= \sum_{n=1}^N y_{t1n}e^{j(n-1)\phi_m}. \end{aligned} \quad (11)$$

A ring oscillator can be studied with the aid of circulant symmetric matrix analysis. Consider an N -stage ring oscillator shown in Fig. 8. Defining a port at the output of each stage, the current flowing through each port can be calculated in terms of the Y-parameters of each stage, $\mathbf{Y}_s = [y_{s_{i,j}}]_{(2 \times 2)}$, that is

$$I_k = y_{s21}V_{k-1} + (y_{s11} + y_{s22})V_k + y_{s12}V_{k+1}. \quad (12)$$

Therefore, from (12), the total admittance matrix of the ring is expressed by

$$\mathbf{Y}_r = \text{circ}(y_{s11} + y_{s22}, y_{s12}, 0, \dots, 0, y_{s21}) \quad (13)$$

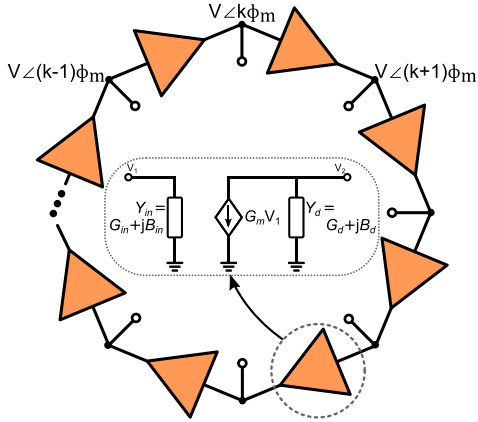


Fig. 9. N -stage ring and schematic of a simple G_m -cell-based stage used in the ring.

then the mode- m input admittance of the ring, $Y_{r,m}$, is readily calculated to be

$$Y_{r,m} = \lambda_{r,m} = y_{s11} + y_{s22} + y_{s12}e^{j\phi_m} + y_{s21}e^{-j\phi_m}. \quad (14)$$

From (14), an oscillation state exists in mode- m if $\text{Re}\{Y_{r,m}\} < 0$ and $\text{Im}\{Y_{r,m}\} = 0$. Considering a simple ring oscillator stage, shown in Fig. 9, we have $y_{s12} = 0$ and $y_{s21} = G_m$. Solving (14) for its real and imaginary parts yields

$$G_m \cos \phi_m + G_{in}(j\omega) + G_d(j\omega) \leq 0 \quad (15)$$

$$\sin \phi_m = \frac{B_{in}(j\omega) + B_d(j\omega)}{G_m}. \quad (16)$$

Frequencies satisfying both (15) and (16) determine the frequency and the mode in which the oscillation states occur. Furthermore, for (15) to hold, $\pi/2 \leq \phi_m \leq 3\pi/2$, and thus, $(1/2) \leq (m/N) \leq 3/4$ and $N \geq 2$. For a general case where $G_{in} + G_d$ is the frequency dependent, the oscillation state with maximum negative conductance at an oscillation frequency satisfying (16) is the strongest oscillation state.

If $G_{in} + G_d$ is frequency independent, the strongest oscillation states occur in the modes with ϕ_m values closest to π , as is evident from (15). Explicitly

$$\arg \min_{0 \leq m \leq N-1} |\phi_m - \pi| = \begin{cases} \frac{N}{2} & \text{for } N = \text{even} \\ \frac{N \pm 1}{2} & \text{for } N = \text{odd.} \end{cases} \quad (17)$$

As implied by (17), for even number of ports, an oscillation state is only possible for mode- $(N/2)$. With an odd number of ports, possible oscillation states occur at mode- $(N \pm 1/2)$.

Similar to what was discussed earlier, assuming an N -port circularly symmetric passive network \mathbf{Y} , an N -port circularly symmetric excitation network $\tilde{\mathbf{Y}}$ exists, which can potentially generate oscillation once it is connected to this circularly symmetric passive network. Since the admittance matrices are both circulant, the eigenvectors of both are described by (10). Therefore, both \mathbf{Y} and $\tilde{\mathbf{Y}}$ are expressed in terms of their eigenvalue matrices Λ and $\tilde{\Lambda}$, and a common eigenvectors matrix \mathbf{U}

$$\mathbf{Y} = \mathbf{U} \Lambda \mathbf{U}^{-1} \quad \tilde{\mathbf{Y}} = \mathbf{U} \tilde{\Lambda} \mathbf{U}^{-1}$$

where $\Lambda = \text{diag}(\lambda_1, \dots, \lambda_N)$ and $\tilde{\Lambda} = \text{diag}(\tilde{\lambda}_1, \dots, \tilde{\lambda}_N)$ are diagonal matrices with their diagonal elements equal to

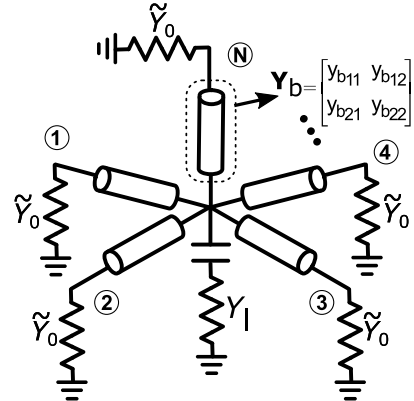


Fig. 10. Schematic of Rucker oscillator.

eigenvalues of \mathbf{Y} and $\tilde{\mathbf{Y}}$, respectively. Consequently, \mathbf{Y}_t can be expressed as

$$\mathbf{Y}_t = \mathbf{U}(\Lambda + \tilde{\Lambda})\mathbf{U}^{-1} \quad (18)$$

revealing that the eigenvalues of \mathbf{Y}_t are diagonal elements of $\Lambda + \tilde{\Lambda}$. Therefore, (6) can be written as

$$\det(\mathbf{Y}_t) = \det(\mathbf{U}(\Lambda + \tilde{\Lambda})\mathbf{U}^{-1}) = 0. \quad (19)$$

For (19) to hold true, at least one value of m must exist such that

$$\lambda_m(j\omega) + \tilde{\lambda}_m(j\omega) = Y_{in,m}(j\omega) + \tilde{Y}_{in,m}(j\omega) = 0. \quad (20)$$

Consequently, (20) implies that the necessary condition for sustainable oscillation at $\omega = \omega_{osc}$ is that these admittances completely cancel out each other at this frequency. Using (11), λ_m can be expressed by

$$\lambda_m = y_{11} + \sum_{n=2}^N y_{1n} e^{j(n-1)\frac{2m\pi}{N}}. \quad (21)$$

Additionally, using (21), λ_{N-m} is calculated

$$\lambda_{N-m} = y_{11} + \sum_{n=2}^N y_{1n} e^{-j(n-1)\frac{2m\pi}{N}}. \quad (22)$$

Furthermore, the reciprocity of the passive network indicates that $y_{ij} = y_{ji}$. Then, inspecting (9) reveals that $y_{1,n} = y_{1,N-n+2}$. Therefore, defining $l = N - n + 2$, (22) is expressed as

$$\begin{aligned} \lambda_{N-m} &= y_{11} + \sum_{l=2}^N y_{1,(N-l+2)} e^{j(l-1)\frac{2m\pi}{N}} \\ &= y_{11} + \sum_{l=2}^N y_{1,l} e^{j(l-1)\frac{2m\pi}{N}} = \lambda_m. \end{aligned} \quad (23)$$

Equation (23) shows that the input admittance of a rotationally symmetric passive is insensitive to direction of the rotation.

The Rucker oscillator [34], [35], shown in Fig. 10, is a special case of this scenario where both excitation and passive networks are of rotational symmetry. In this oscillator, the excitation network consists of N identical negative-resistance diodes. Assuming the admittance of each diode to be \tilde{Y}_0 , from the discussion in Section II-A, we infer that

$\tilde{Y}_{\text{in},m} = \tilde{\lambda}_m = \tilde{Y}_0$. The passive network of this oscillator is comprised of N identical two-port passive sub-networks (e.g., transmission lines) connected to a central common node, as shown in Fig. 10. A load with an admittance of Y_l is connected between this common node and ground. In this “star-shaped” configuration, the relation between each port to all other ports is identical, and thus, the elements of the admittance matrix are

$$y_{i,j} = \begin{cases} Y_p & \text{if } i = j \\ Y_{pp} & \text{if } i \neq j. \end{cases}$$

The mode- m input admittance of the passive network (i.e., the m th eigenvalue of \mathbf{Y}) is readily calculated from (5) and (11) to be

$$\begin{aligned} Y_{\text{in},m} &= \lambda_m = Y_p + \sum_{n=1}^{N-1} Y_{pp} e^{jn\phi_m} \\ Y_{\text{in},m} &= \begin{cases} Y_p + (N-1)Y_{pp} & \text{if } m = 0 \\ Y_p - Y_{pp} & \text{if } m \neq 0. \end{cases} \quad (24) \end{aligned}$$

Using (20), (24) reveals that for an oscillation state to occur, $\tilde{Y}_0 = -Y_{\text{in},m}$. Each branch of the star is a two-port passive network with $\mathbf{Y}_b = [y_{b,i,j}]_{(2 \times 2)}$ representing the Y-parameters of each branch. Y_p and Y_{pp} are then readily obtained, that is

$$\begin{aligned} Y_p &= y_{b11} - \frac{y_{b12}^2}{Ny_{b22} + Y_l} \\ Y_{pp} &= -\frac{y_{b12}^2}{Ny_{b22} + Y_l}. \quad (25) \end{aligned}$$

Plugging (25) into (24) yields the closed-form expression for $Y_{\text{in},m}$

$$Y_{\text{in},m} = \begin{cases} y_{b11} - \frac{y_{b12}^2}{y_{b22} + Y_l/N} & \text{if } m = 0 \\ y_{b11} & \text{if } m \neq 0. \end{cases} \quad (26)$$

Inspection of (26) reveals that for mode-0 or the so-called “in-phase” mode, the load impedance is scaled up by N times, and transferred to the input of each branch. This is as if each branch is disconnected from the common node and sees $1/N$ th of the load at its output. Furthermore, for any $m \neq 0$, we expect the common node to act as virtual ground due to symmetry of the structure, and thus, $Y_{\text{in},m} = y_{b11}$. It is thus inferred that as long as $\text{Re}\{y_{b11} - (y_{b12}^2/y_{b22} + Y_l/N)\} < \text{Re}\{y_{b11}\}$ for all frequencies, \tilde{Y}_0 can be chosen, such that oscillation states occur only in mode-0 at oscillation frequencies ω_0 , where $\text{Im}\{Y_{\text{in},m}(j\omega_0) + \tilde{Y}_0(j\omega_0)\} = 0$.

In this paper, we extend the theorem and analysis of multi-port circulant oscillators to design and optimize a circular-cavity-based oscillator.

III. MULTI-PORT PASSIVE NETWORK DESIGN: AN EIGHT-PORT CIRCULAR CAVITY

Cavity resonators realized by enclosing rectangular or circular waveguides are known for their high quality factor (Q) [36]. References [13] and [37]–[41] studied the design and implementation of substrate-integrated waveguides in silicon technologies. The multi-port passive structure, in this

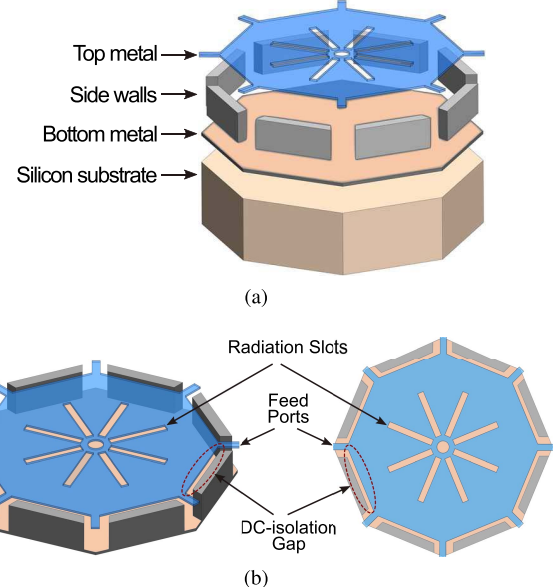


Fig. 11. Octagonal cavity implemented using the metal stack of a 0.13- μm SiGe BiCMOS process. (a) Stack-up. (b) 3-D structure and top view.

paper, is an octagonal-shaped circular cavity realized using the metal stack available in a 0.13- μm BiCMOS process, as shown in Fig. 11(a). It is comprised of eight symmetric feed ports, eight radiation slots on the top plate, and a hole at the center of the top plate [see Fig. 11(b)]. Its inherent high Q -factor is exploited to achieve high-power and low-phase-noise operation. Moreover, a hole is created at the center of the top plate to manipulate the cavity resonances. Section III-A will further describe the role of this hole in suppressing the unwanted resonances. Eight co-planar waveguide (CPW)-based feed ports are placed on the periphery of this cavity and are connected to the top plate to excite it, enabling power-combining capability within this multi-port cavity structure. Moreover, eight rotationally symmetric slots are created on the top plate for the circularly polarized radiation. A slot gap is implemented between the top plate and the sidewalls to provide dc isolation between the feed ports and the ground, which was necessary for proper operation of the excitation active circuit. Otherwise, high-quality dc block caps would have been needed in series with the feed ports. The low Q -factor and self-resonance frequency of such capacitors would directly degrade the efficiency of the oscillator. This slot gap also contributes to circularly polarized radiation, as will be discussed in Section III-B.

A. Characterizing Cavity Resonances

A cavity resonator, as a 3-D enclosed distributed structure, contains multiple resonances in TE or TM mode, each one corresponding to a unique distribution of EM fields inside the cavity. The resonant frequencies depend on the geometric dimensions and the dielectric material that fills the cavity volume. Excitation of each resonance requires a specific set of excitation waves at the cavity feed ports compatible in phase and spatial direction with the field distribution of that particular resonance at the port boundaries. As mentioned earlier, excitation ports of the proposed on-chip cavity employ CPW-based feed lines. Thus, among all possible resonances

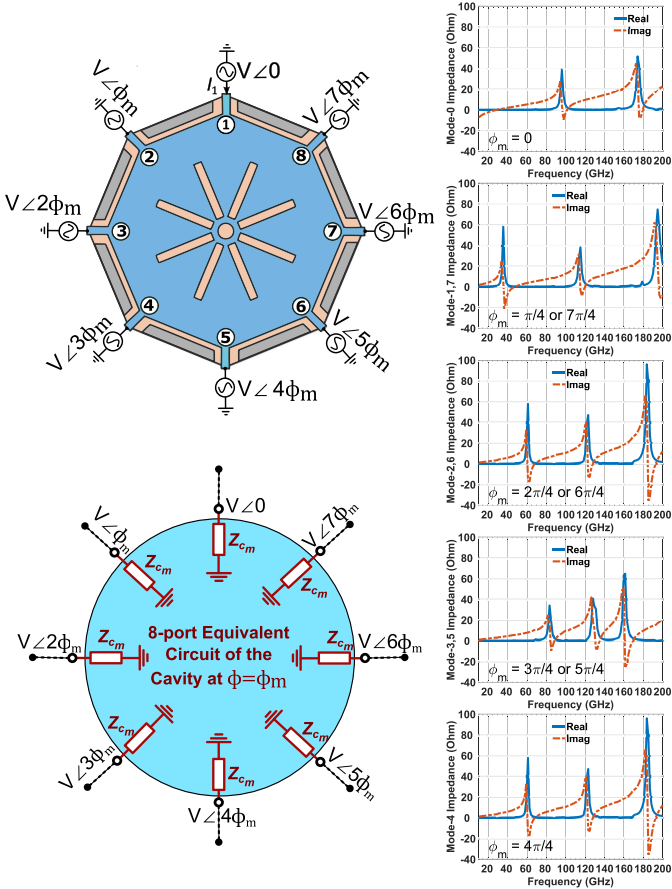


Fig. 12. Cavity input impedances associated with different modes.

existing in the cavity structure, those that can be excited by the EM modes supported by the CPW feed lines are subject to this paper. Moreover, we only focus on the resonance modes excited by applying the CPW TEM mode at the feed ports, as the cutoff frequency of higher modes of these CPW feed lines is much higher than the frequency range of interest. Finally, as the cavity is connected to a circularly symmetric excitation network, for this resultant network to oscillate, the analysis in Section II-B concludes that the port voltages should be proportional to one of the \bar{U}_m values given by (10) associated with mode- m . Therefore, port boundary conditions of interest narrow down to those whose corresponding port voltage vectors are proportional to \bar{U}_m 's. As a result, all ports of this eight-port cavity attain the same voltage amplitude V_a and phase difference ϕ_m between its adjacent ports, where $\phi_m = 2\pi (m/8)$.

To characterize the mode- m input impedance of the cavity, $Z_{c,m} = (1/Y_{c,m})$, excitation signals proportional to \bar{U}_m are thus applied at the cavity feed ports. Rotational symmetry of the structure yields circulant impedance/admittance matrices. Hence, the mode- m input admittance of the cavity is derived using (21). Furthermore, the reciprocity and rotational symmetry of the cavity [see (23)] necessitates that the eight distinct modes can only lead to five distinct mode input impedances associated with $m = 0, 1$ (or 7), 2 (or 6), 3 (or 5), and 4 . Fig. 12 shows the mode- m input impedance for $m = 0, \dots, 4$. Examining these $Z_{c,m}$ values reveals that for each value of m , the cavity exhibits a resonance behavior at distinct frequencies

$\omega_{m,i} = 2\pi f_{m,i}$ (for $i = 1, 2, \dots$). Each resonant frequency is associated with one of the TE or TM mode resonances of the cavity, which is excitable by the EM field generated by the excitation signals of mode- m at the feed ports. Distinct resonance behaviors arise for different values of m , as the boundary conditions forced by the excitation signals to the ports of the cavity are dependent on ϕ_m . Moreover, the resonance frequencies are mainly controlled by the cavity's planar dimensions [36], as its maximum vertical height (determined by the metal stack thickness) is significantly smaller due to the silicon process constraints.

To design a single-state oscillator, only one of the cavity resonances is allowed to be excited. Therefore, it is desirable to design an excitation network, which exhibits a narrow-band negative resistance around the resonance frequency of interest. On the other hand, only excitation signals associated with mode-1 and mode-7 can generate circularly polarized radiation in a rotationally symmetric radiator, as will be illustrated in Section III-B. Excitation in one of these two modes leads to the left-hand circularly polarized radiation with the other one leading to the right-hand radiation. As explained earlier, the mode input impedances of these two modes are indistinguishable from one another. Excitation by a simple structure of eight identical single-element negative resistors (Section II-A) results in concurrent appearance of these two oscillation states, which significantly distort the resultant polarization. Consequently, the excitation network must be designed to provide sufficiently large negative resistance to the cavity only for one of these two modes while providing either a positive or a much weaker negative resistance for the other one (see Section IV).

Fig. 14 shows the mode input impedance $Z_{c,1} = Z_{c,7} = Z_{c,17}$ corresponding to mode-1 and mode-7 for frequencies up to 160 GHz, a frequency range below f_{\max} , where the device can provide sufficient output power. Fig. 14 also shows the existence of two resonances for each mode. In this design, the second resonant frequency of these modes located at 116 GHz is selected, since it lies within the frequency range, where the gain of the circularly polarized radiation is sufficiently high (e.g., ≈ 1 dBi), i.e., $f_{1,2} = f_{\text{rad}} = 116$ GHz. At the same time, the radiation gain at the first resonant frequency is much lower at -25 dBi. The cavity radiation mechanism and its characteristic will be explained in Section III-B, where the selection of the second resonant frequency will also be quantified.

An important notion is the existence of unwanted resonant frequencies for modes other than mode-1 and mode-7, which are close to f_{rad} . This would exert stringent requirement on the frequency selectivity and high Q -factor of the excitation network. In particular, mode-0 input impedance $Z_{c,0}$ contains strong resonance very close to f_{rad} , which leads to an undesired in-phase oscillation once the cavity is connected to the excitation network. This close proximity mandates an excitation network with a Q -factor in the range of 100 to suppress it! An alternative way to suppress this strong in-phase oscillation is by making structural changes to the cavity in order to alter the EM field distribution for this specific unwanted resonance. One can observe from EM simulations

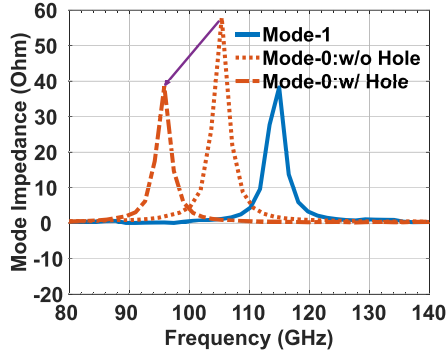


Fig. 13. Resonances associated with mode-1, and mode-0 with and without the hole at the center of cavity.

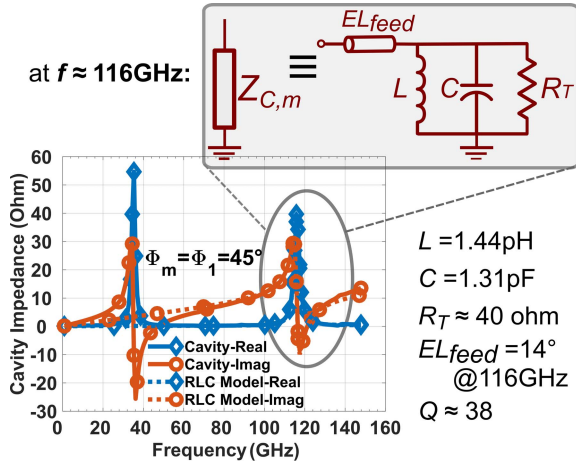


Fig. 14. Simulated cavity impedance associated with mode-1 and the RLC lumped circuit that models the cavity resonance in this mode at 116 GHz.

that the field intensity for this undesired resonance associated with mode-0 is non-zero at the center of the cavity, while it is zero for resonances associated with other modes due to symmetry of the structure. This observation implies that metallic structures can be added to or removed from the center of the cavity to significantly attenuate the in-phase resonance in the vicinity of f_{rad} without having significant impact on desired resonance. It has then been discovered that opening a hole at the center of the cavity shifts this resonant frequency of the in-phase mode (mode-0) to a lower frequency and effectively lowers the mode-0 impedance, while the resonance and the radiation of the other modes remain almost unaffected due to their odd symmetry (see Fig. 13). To gain intuitive understanding about the behavior of the desired resonance associated with mode-1, its impedance can be approximated by that of a lumped RLC circuit at the vicinity of f_{rad} , as shown in Fig. 14. The component values of the circuit model can be obtained by curve fitting the model impedance to the mode-1 cavity impedance calculated from the cavity's EM simulation data. The RLC model reveals an equivalent capacitance of 1.3 pF and a shunt tank resistance of 40 Ω leading to Q of 38, which is quite high for a radiating element at this frequency.

B. Radiation Characteristic

This multi-port cavity-backed antenna radiates through eight symmetric slots on its top plate. The length of the slots controls its resonant frequency and, thus, the frequency of the

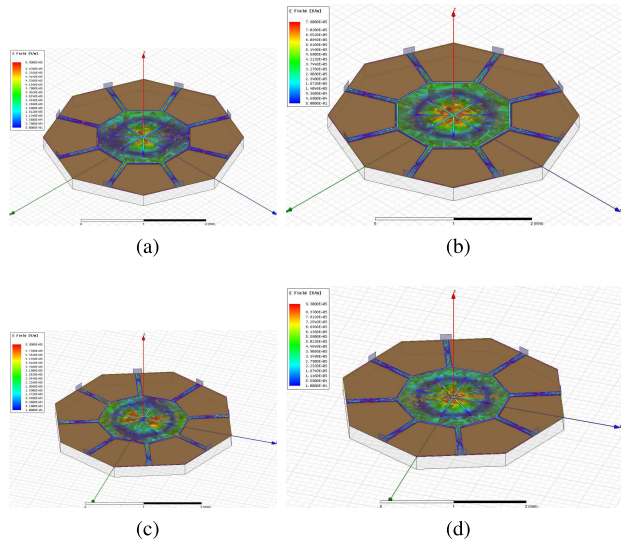


Fig. 15. E -field magnitude distribution inside the cavity for (a) mode-1 at 116 GHz without the hole at the center, (b) mode-0 at 106 GHz without the hole at the center, (c) mode-1 at 116 GHz with the hole at the center, and (d) mode-0 at 96 GHz with the hole at the center.

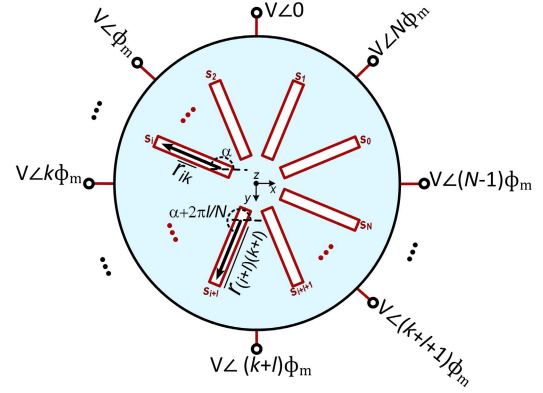


Fig. 16. Generation of circularly polarized radiation by exciting a rotationally symmetric multi-port radiator using RF signals with distinct evenly spaced phases.

peak radiation gain. Their distance and orientation (angular location) with respect to the feed ports is chosen, such that around the desired resonant frequency associated with mode-1, the E -field vector assumes its peak magnitude close to the center of each slot. Fig. 15 shows the E -field distribution of the desired mode as well as mode-0 inside the cavity with and without the center hole in conjunction with the locations of the slots. The slot widths control the radiation resistance, which impacts the radiation gain. They also affect the cavity mode-1 input impedance and impact the Q -factor of the desired resonance. As a result, the cavity dimension and slot sizes are co-designed to provide an acceptable radiation gain while reducing the cavity loading effect on the surrounding excitation network.

Theorem 1: Consider an N -port passive radiating structure with rotational symmetry incorporating N rotationally symmetric radiating slots and feed ports, as shown in Fig. 16. Suppose that the feed ports are excited by the signals of equal magnitude and constant phase shift of $2\pi/N$. Such a structure will generate circularly polarized radiation along its axis of symmetry (z).

Proof: According to Fig. 16, the excitation signals have equal magnitude and constant phase shift of $\phi = 2\pi m/N$ (i.e., $V_k = V_0 e^{j2\pi(k-1)m/N}$, $1 \leq k \leq N$). The excitation voltages create an E -field at the location of each slot s_i which, in turn, can be modeled by an effective magnetic current-density vector \bar{M}_i as the radiation source associated with s_i [23]. The excitation voltage at each feed port, V_k , contributes linearly to the generation of \bar{M}_i . The weighting coefficient of this contribution is defined by a complex vector $\bar{r}_{ik} = (\bar{M}_i/V_k)|_{V_l \neq 0}$ whose direction is determined by the position of s_i relative to the k th port. \bar{M}_i is then expressed as

$$\bar{M}_i = \sum_{k=1}^N \bar{r}_{ik} V_k = \sum_{k=1}^N \bar{r}_{ik} V_0 e^{j(k-1)\frac{2\pi m}{N}}. \quad (27)$$

Because of the circular symmetry and the reciprocity of the structure, the effective magnetic current-density vector created by V_k at s_i referenced to the k th port is the same as that created by V_{k+l} at s_{i+l} referenced to the $(k+l)$ th port. Therefore, considering a fixed reference point located at the center of the structure, these two magnetic current-density vectors are the same but with spatial angular rotation of $2\pi l/N$, that is

$$r_{(i+l)(k+l)} = R_{l\frac{2\pi}{N}}(r_{ik}) \quad (28)$$

where $R_{l\frac{2\pi}{N}}(\cdot)$ defines an operator function which rotates a vector around the z -axis by $l\frac{2\pi}{N}$. For $\phi_m = \pm 2\pi/N$ (i.e., $m = \pm 1$), and using (27) and (28), it is seen that

$$\bar{M}_{i+l} = R_{l\frac{2\pi}{N}}(\bar{M}_i) e^{jl\frac{2\pi}{N}}. \quad (29)$$

Equation (29) indicates that for radiative slots with $\phi = 2\pi l/N$ angular rotation in space, their effective magnetic current-density vectors will exhibit the same angular rotation in space and also the same angular difference in time. Each \bar{M}_i creates an E -field \bar{E}_i on the z -axis, such that $\bar{E}_i = \mathbf{A}_i \bar{M}_i$, where \mathbf{A}_i is the tensor mapping \bar{M}_i to \bar{E}_i . Given the rotational symmetry of the structure, all \mathbf{A}_i values are equal on the z -axis. Therefore, using (29), the total E -field $\bar{E}_{\text{tot}} = \sum_{i=1}^N \bar{E}_i$ is expressed as

$$\bar{E}_{\text{tot}} = \sum_{i=0}^{N-1} R_{i\frac{2\pi}{N}}(\bar{M}_1) e^{ji\frac{2\pi}{N}} = \sum_{i=0}^{N-1} R_{i\frac{2\pi}{N}}(\bar{E}_1) e^{ji\frac{2\pi}{N}}. \quad (30)$$

Equation (30) reveals that E_{tot} is the summation of E -field vectors with equal magnitude and equally spaced angular rotation and phase shift. This, in turn, provides the necessary and sufficient condition for circularly polarized radiation [23]. \square

Theorem 1 clearly states that the circular cavity in Fig. 11(a) is capable of producing circularly polarized radiation if excited by the signals of equal amplitude and constant phase shift of $2\pi/N$. Either one of the two excitations corresponding to $\pm 2\pi/8$ leads to a left- or right-hand polarization radiation.

As was briefly discussed at the beginning of this section, a slot gap exists within the structure of this eight-port cavity between the top plate and the sidewalls. This slot gap acts as a capacitive termination at the boundaries of this cavity. This is in clear contrast with conventional cavity structures [36], where sidewalls are short circuited to the top and bottom

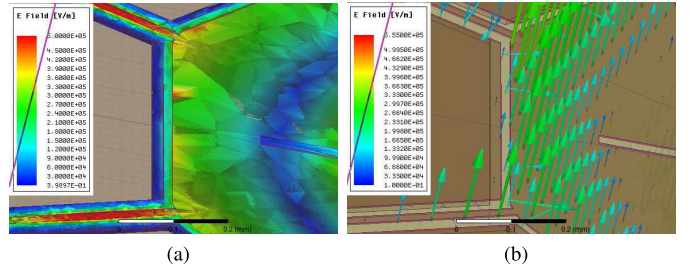


Fig. 17. (a) Magnitude and (b) vector distribution of E -field inside the cavity at the vicinity of the top plate gap.

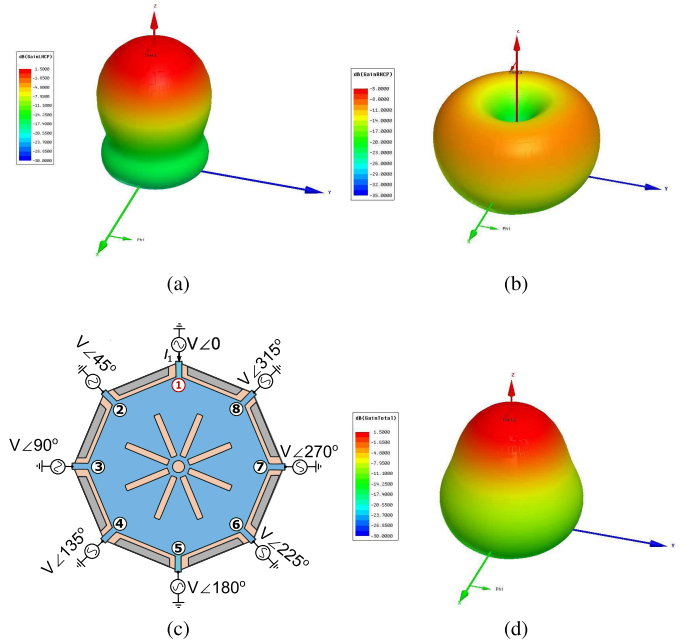


Fig. 18. (a) Left-hand side and (b) right-hand side circularly polarized radiation. (c) Corresponding excitation phases. (d) Total radiation pattern.

plates. The open-circuit boundary in this cavity facilitates the formation of a peak in the E -field magnitude underneath the top plate right at the location of the gap, which also contributes to radiation into the free space. The two simulation plots in Fig. 17(a) and (b) show the E -field distribution inside the cavity at 116 GHz in the vicinity of the gap when the cavity is excited in mode-1. The E -field magnitude plot in Fig. 17(a) shows the formation of an open circuit right at the gap location. The vector distribution plot in Fig. 17(b) shows the traverse E -field across the gap, which leads to radiation from the gap. This radiation is also circularly polarized, according to Theorem 1.

Fig. 18 shows that for $\phi_m = 2\pi/8$, the antenna will provide a gain of 1.25 dB with the right-hand circular polarization.

IV. MULTI-PORT RING OSCILLATOR DESIGN

To simultaneously excite all eight ports of the cavity by oscillatory signals with a phase difference of $2\pi/8$, an eight-stage ring oscillator is designed, as shown in Fig. 20(a). The ring topology has the capability of distinguishing between clockwise and counterclockwise phase progression, as the amplifiers within the ring stages are unidirectional. As mentioned in Section III, this attribute of the excitation network is required for preventing dual-mode operation when the passive

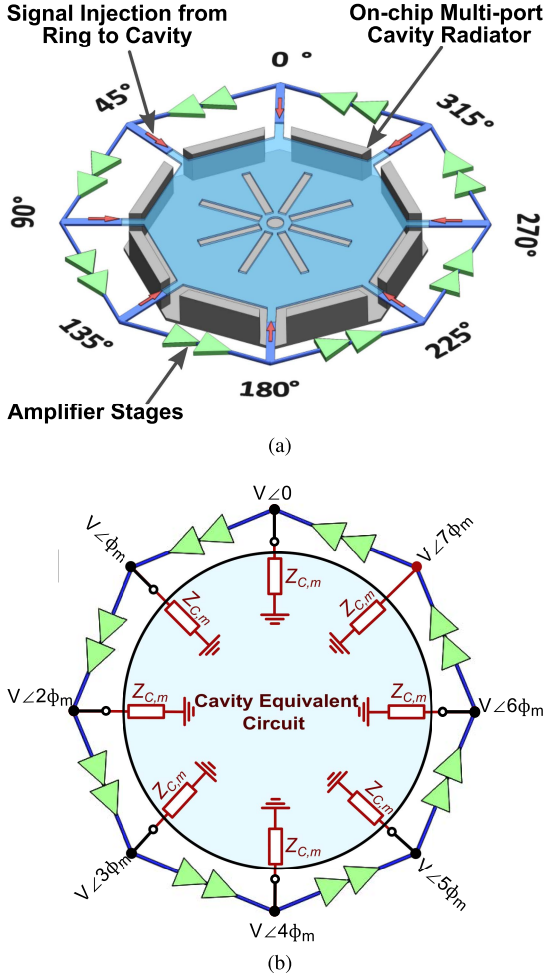


Fig. 19. (a) Multi-port cavity-backed circularly polarized radiator architecture. (b) Ring oscillator loaded by the cavity.

network is of circular symmetry. To analyze the oscillation start-up condition for each oscillation state, the cavity is replaced by its equivalent eight-port network, where its mode- m input impedance $Z_{c,m} [= 1/Y_{c,m} = 1/\lambda_m]$ and λ_m is given by (11)] captures the loading effect on each port of the ring oscillator [Fig. 20(b)]. Section III-A showed that $Z_{c,m}$ exhibits multiple resonances for each m , and the resonant frequency of 116 GHz associated with $m = 1$ or 7 is chosen for oscillation due to its capability of generating circularly polarized radiation, as described in Section III-B. Assuming that each section of the ring is described by its Y-parameters, the admittance looking into each port of the ring is then expressed by (14). The analysis then follows by considering the ring oscillator as the excitation network and the circular cavity as the passive network. In light of the terminology used in Section II, $\tilde{\lambda}_m = Y_{r,m}$ and $\lambda_m = Y_{c,m}$. The main goal in designing the amplifier stages within the ring is then to satisfy the oscillation start-up condition given by (20) only for $m = 1$ and at the target frequency of $f_{osc} \simeq 115$ GHz,¹

¹One can alternatively choose $m = 7$ and design the ring for the same oscillation frequency. The only difference would be the polarization direction of the radiated wave.



Fig. 20. Block-level schematic of amplifier stage within the ring oscillator.

and suppress undesired oscillation states at any other mode ($m \neq 1$) or frequency. Consequently, the desired behavior of the total admittance $Y_{t,m}$ is expressed as

$$\begin{cases} \operatorname{Re}\{Y_{t,m}(j\omega = j\omega_{osc})\} < 0 \\ \operatorname{Im}\{Y_{t,m}(j\omega = j\omega_{osc})\} = 0 \quad \text{for } m = 1 \\ \operatorname{Re}\{Y_{t,m}(j\omega = j\omega)\} > 0 \quad \text{for } m \neq 1 \end{cases} \quad (31)$$

where $\omega_{osc} = 2\pi \times f_{osc}$ is the target oscillation frequency. The cavity mode- m input admittance is derived from its Y-parameters (extracted from the full-wave EM simulations carried out in ANSYS HFSS) and (11). Therefore, using (31), the constraints on mode- m input admittance of the ring is obtained as follows:

$$\begin{cases} \operatorname{Re}\{Y_{r,m}(j\omega_{osc})\} < -\operatorname{Re}\{Y_{c,m}(j\omega_{osc})\} \\ \operatorname{Im}\{Y_{r,m}(j\omega_{osc})\} = -\operatorname{Re}\{Y_{c,m}(j\omega_{osc})\} \quad \text{for } m = 1 \\ \operatorname{Re}\{Y_{r,m}(j\omega) + Y_{c,m}(\omega)\} > 0 \quad \text{for } m \neq 1. \end{cases} \quad (32)$$

It is noteworthy that the first two conditions in (32) are to be met exclusively for a specific ω_{osc} . Otherwise, an unwanted oscillation state at a different frequency but in the same mode, mode-1, occurs.

Fig. 20 shows the block-level schematic of each stage of the amplifier. Two common-emitter (CE) amplifiers are employed within each stage to provide gain for sustainable oscillation. Also, three two-port networks, namely input-, inter-stage, and output- passive-networks, are shown in Fig. 20, which are employed to adjust the admittance of each stage, \mathbf{Y}_s , so as to meet the oscillation conditions specified in (32) for single-state oscillation at ω_{osc} .

The CE transistors, $Q_{1,2}$ are biased at the current density corresponding to maximum f_{max} and are sized to deliver maximum output power at 115 GHz after parasitic extraction, including the contact parasitics up to the top metal. This procedure is conducted by cycling through several iterations of device layout, EM simulation of contacts, and harmonic-balance simulations. Reference [7] showed that the transistors, as two-port networks, can generate their maximum RF power when the complex voltage gain of the device, A_v , attains a frequency- and bias-dependent optimum value $A_{opt} = A_0 e^{j\phi_{opt}}$. The phase of A_{opt} is mainly determined by the device parasitics such as C_μ , which rotates the phasor of total collector current relative to that of the transistor transconductance current. A_0 is mainly affected by the large-signal behavior, including transistor nonlinearity as well as voltage clipping due to limited supply voltage. Fig. 21(a) shows the test bench used to obtain A_{opt} , where RF voltage sources $V_b \sin(\omega_0 t)$ and $V_c \sin(\omega_0 t + \phi)$ drive base and collector terminals of the transistor, respectively, and the total output power P_{out} generated by the transistor is measured. The base and collector RF amplitudes, V_b and V_c , as well as the phase difference between the two, ϕ , are then varied with respect to the

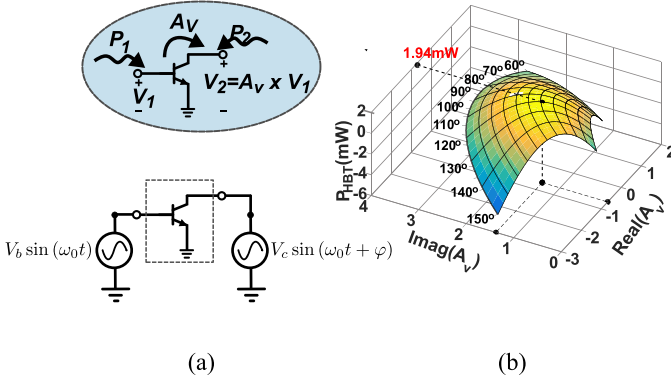


Fig. 21. (a) Simulated test bench used for finding maximum output power of a transistor. (b) Transistor output power versus complex voltage gain.

supply and bias limitations on each terminal. The maximum achievable output power and the optimum voltage gain are found exhaustively

$$\begin{aligned} P_{\max} &= \max(P_{\text{out}}) \\ A_{\text{opt}} &= A_0 e^{j\varphi_{\text{opt}}} = \frac{V_c}{V_b} e^{(j\varphi)} \quad \text{where } P_{\text{out}} = P_{\max}. \end{aligned} \quad (33)$$

Fig. 21(b) shows the simulated \$P_{\text{out}}\$ versus \$A_V\$. It is seen that for \$A_V \approx 1.4 \angle 85^\circ\$, \$P_{\text{out}}\$ is maximized. References [7] and [8] have used local feedback networks across the transistor to reach optimum voltage-gain condition for the device. However, the use of an inductor [25], [42] or a high-impedance t-line [7] was found to be necessary for maximizing \$P_{\text{out}}\$. In this design, we first found out that such high-impedance on-chip t-lines are quite lossy, thereby degrading dc-to-EIRP conversion efficiency. Furthermore, we observed that a global feedback exists within the ring oscillator structure, which forces the phase shift per stage according to the mode of the dominant oscillation state. This property was exploited to satisfy the optimum voltage gain condition. Consequently, to extract maximum oscillation power at the desired state (mode-1 and \$\omega_{\text{osc}} = 2\pi \times 115\$ GHz), the passive networks are designed, such that at the vicinity of \$\omega_{\text{osc}}\$, each device experiences a voltage gain close to \$A_{\text{opt}}\$ across its base and collector when the voltage at the input and output terminals of each stage is of equal amplitude and phase difference \$\phi_m = 2\pi/8\$ in accordance with the desired oscillation state.

The complete schematic of each stage of the ring is shown in Fig. 22. The passive networks are implemented using t-line-based T-sections with their short stubs providing dc bias path, and interdigitated capacitor \$C_s\$ for dc isolation besides shaping the frequency response. More specifically, \$C_s\$ heavily attenuates the low-frequency loop gain and suppresses the associated oscillation states. The self-resonance of \$C_s\$ caused by the delay due to the finite length of their fingers is modeled using two series t-lines, as shown in Fig. 24(a), each with a length almost equal to half of the capacitor physical length, which are then absorbed into the t-lines of the T-sections. Base-side short stubs are terminated with a \$C\$-\$RC\$ network, as shown in Fig. 24(b). \$R_1\$-\$C_1\$ and \$R_2\$-\$C_2\$ branches guarantee low-frequency stability of the structure, while \$C_B\$, which is implemented as a stacked interdigitated capacitor with the self-resonance frequency of 130 GHz, provides the high-frequency decoupling.

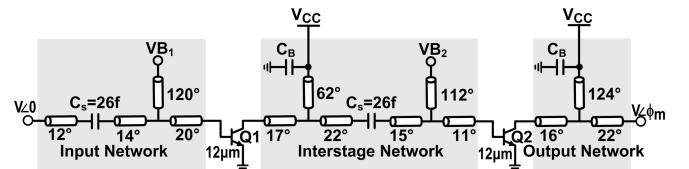


Fig. 22. Schematic of amplifier stage within the ring.

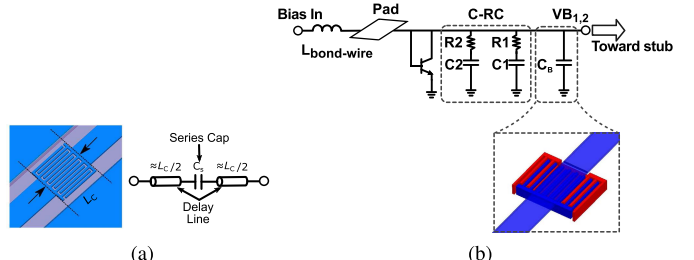


Fig. 23. (a) Series interdigitated capacitor and its model. (b) Bias decoupling network.

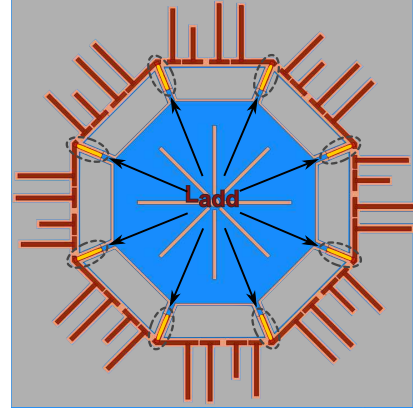


Fig. 24. T-line, \$L_{\text{add}}\$, added to the cavity feed port to adjust the total length of the passives within the ring.

Besides oscillation performance objectives, geometrical constraints are also of vital importance and are considered in the design process. More specifically, since the ring is placed around the multi-port circular cavity, the total length of eight stages, including the transistors, capacitors, and the t-lines, should exactly be equal to the periphery of the cavity. Realizability and loss of the passives used in satisfying the design objectives is a key point in the implementation of this multi-port oscillator. Having a fixed total length for the ring passives imposes strict constraints to the extent that design objectives cannot be satisfied. To remove this geometry-imposed restriction, eight t-lines, \$L_{\text{add}}\$, are placed between corresponding ports of the cavity and the ring (see Fig. 24). This, in turn, removes the tight constraint on the length of the ring's passives and helps in achieving optimum gain condition. Note that this extra t-line rotates the impedance seen from the cavity, thereby slightly shifting the resonant frequency. Moreover, its associated loss degrades the oscillator efficiency. Nevertheless, the additional degree of freedom due to its use is still beneficial in satisfying these optimum conditions.

Finally, the choice of two CE amplifiers within each stage, which is made in light of power and efficiency optimization of the oscillator, can be justified as follows.

For ring stages with a single CE transistor, we found that the optimal lengths of the ring passives satisfying the oscillation performance objectives alone (i.e., ignoring the geometrical

restrictions) significantly differ from the values obtained from geometrical constraints. More specifically, the interconnects required for delivering the signal to the cavity ports in this scenario are excessively long, leading to poor output power and dc-to-EIRP conversion efficiency. In other words, the area available around the cavity is not efficiently utilized for signal generation and amplification. On the other hand, the use of two CE amplifiers per each stage allows for the total lengths of the ring passives to become closer to the perimeter of the cavity. In the meantime, extracting maximum RF power from the first CE transistor results in higher available power from the second CE transistor to be delivered to the cavity. Therefore, both transistors almost equally contribute to the power delivered to the cavity.

Fig. 26(a) shows simulated $Y_{t,m}$ for $m = 0, \dots, 7$. It is seen that the $\text{Re}\{Y_{t,m}\}$ is positive across frequency for all values of m except $m = 1$, where the admittance goes outside the Smith chart. For $m = 1$, the real and imaginary parts of $Y_{t,m}$ are plotted in Fig. 26(b), indicating a resonance at 115 GHz in addition to a narrow-band negative resistance around this frequency. To verify the transistor optimum voltage-gain condition, the ac voltage gain across each transistor is also plotted in Fig. 26. Using Spectre simulations, it is verified that a stable oscillation takes place at $m = 1$, as the steady-state waveforms of port voltages shown in Fig. 28(a) are 45° apart. The transient voltage waveforms of the transistors base and collector terminals, shown in Fig. 28(b), also verify the optimum voltage-gain condition in large-signal operation.

The base bias is varied to achieve frequency tuning, mainly by changing C_π of the HBT transistors. Fig. 29 shows the oscillation frequency and output power versus the base bias current, indicating more than 1 GHz of tuning range.

V. OSCILLATION STABILITY OF MULTI-PORT OSCILLATORS

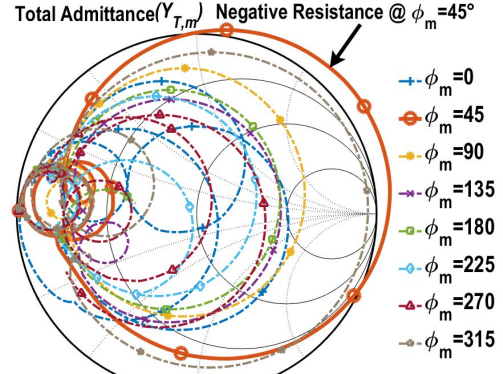
In this section, the requirements and the conditions for stability of an oscillation state in a multi-port oscillator are studied. To identify the necessary and sufficient conditions, a small perturbation is applied to an oscillator operating in one of its oscillation states, and the oscillator response is analyzed. Inspired by the study conducted in [32], we extend the stability analysis to the general case of an N -port excitation network with no restrictive assumption about topological nature of active and passive components. We will then apply this general theory on the special case of circular symmetric oscillators.

Suppose that for a multi-port oscillator, an oscillation state at oscillation frequency ω_{osc} exists in mode- m of the total network. Equations (2) and (5) will, therefore, lead to

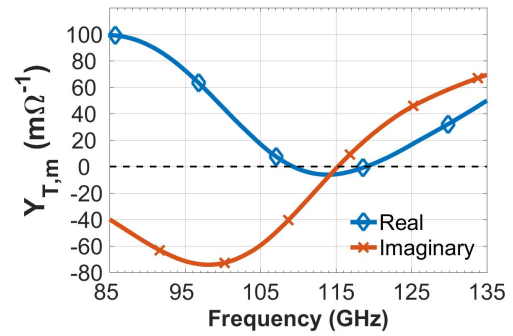
$$Y_{t,m_k}(\omega_{\text{osc}}, \bar{V}) = Y_{m_k}(\omega_{\text{osc}}, \bar{V}) + \tilde{Y}_{m_k}(\omega_{\text{osc}}, \bar{V}) = 0 \\ k = 1, \dots, N. \quad (34)$$

As defined before, Y_{t,m_k} represents the mode- m input admittance of the total network. Y_{m_k} and \tilde{Y}_{m_k} are the k th port input admittances of the passive and excitation networks in mode- m , which are expressed as

$$Y_{m_k} = \sum_{i=1}^N y_{k,i} \frac{V_{m_i}}{V_{m_k}} \quad (35)$$



(a)



(b)

Fig. 25. (a) Simulated total admittance of the ring for all modes and (b) its real and imaginary part for $m = 1$.

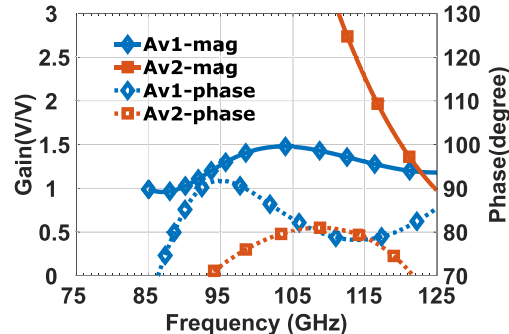


Fig. 26. Simulated voltage gain across each transistor.

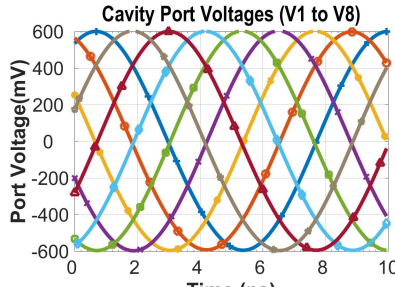
$$\tilde{Y}_{m_k} = \sum_{i=1}^N \tilde{y}_{k,i} \frac{V_{m_i}}{V_{m_k}} \quad (36)$$

where $y_{k,i}$ and $\tilde{y}_{k,i}$ are the elements of \mathbf{Y} and $\tilde{\mathbf{Y}}$. V_{m_k} is the voltage of the k th port in mode- m . Under the assumption of slow variation for its amplitude and phase, V_{m_k} is expressed in the time domain as

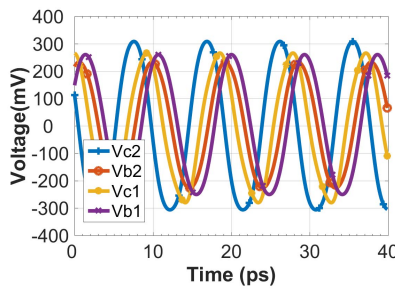
$$V_{m_k} = A_{m_k}(t) e^{(j\omega_{\text{osc}} t + \psi_{m_k}(t))} = A_{m_k}(t) e^{j\theta_{m_k}(t)} \quad (37)$$

where θ_{m_k} is the instantaneous phase of the k th port. $A_{m_k}(t)$ and $\psi_{m_k}(t)$ represent the slowly varying amplitude and phase of each port.

Assuming that \bar{A}_m and $\bar{\Theta}_m$ are steady-state amplitude and phase vectors of port voltages, and \bar{a}_m and $\bar{\delta}_m$ represent their corresponding additive perturbations. Following the approach



(a)



(b)

Fig. 27. (a) Simulated time-domain voltage waveforms of all ports. (b) Simulated transistors terminal voltages.

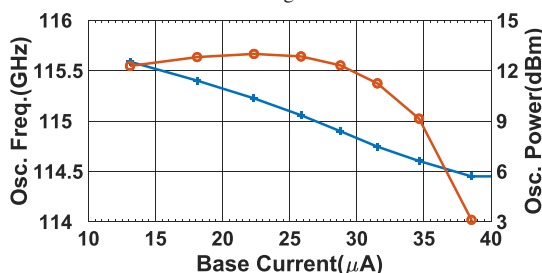


Fig. 28. Oscillation frequency and output power versus base bias current.

taken in [32], we have:

$$\begin{aligned} \dot{a_m}_k &= A_{m_k} \sum_{l=1}^N \operatorname{Im} \left\{ \frac{\partial \Upsilon_{m_k}}{\partial A_{m_l}} \Big|_{\bar{A}_m} a_l + \frac{\partial \Upsilon_{m_k}}{\partial \theta_{m_l}} \Big|_{\bar{\Theta}_m} \delta_l \right\} \\ \dot{\delta_m}_k &= - \sum_{l=1}^N \operatorname{Re} \left\{ \frac{\partial \Upsilon_{m_k}}{\partial A_{m_l}} \Big|_{\bar{A}_m} a_l + \frac{\partial \Upsilon_{m_k}}{\partial \theta_{m_l}} \Big|_{\bar{\Theta}_m} \delta_l \right\} \quad k = 1, \dots, N \end{aligned} \quad (38)$$

where $\dot{a_m}_k$ and $\dot{\delta_m}_k$ present the time derivative of a_{m_k} and δ_{m_k} , respectively. In (38), Υ_{m_k} is defined as

$$\Upsilon_{m_k}(\bar{A}_m, \bar{\theta}_m) = \frac{Y_{t,m_k}}{\partial Y_{t,m_k}/\partial \omega} \Big|_{\omega_{osc}}. \quad (39)$$

The set of equations given by (38) is expressed in its matrix form as follows:

$$\begin{bmatrix} \dot{\bar{a}_m} \\ \dot{\bar{\delta}_m} \end{bmatrix} = \mathbf{M}_m \begin{bmatrix} \bar{a}_m \\ \bar{\delta}_m \end{bmatrix}. \quad (40)$$

For an oscillation state to be stable, the oscillator response to phase and amplitude perturbations must decay with time. For this to occur, all eigenvalues of \mathbf{M}_m should attain negative real parts.

A. Stability Analysis of Circularly Symmetric Oscillators

Using the above general analysis, the oscillation stability conditions of a circularly symmetric oscillator are derived in terms of its passive and excitation network parameters. We define a two-element vector $\bar{\mathbf{P}}_{m_k}$ whose first and second elements are amplitude and phase of the steady-state port voltages for an oscillation state in mode- m , V_{m_k}

$$\bar{\mathbf{P}}_{m_k} = (A_{m_k}, \Theta_{m_k}) \implies V_{m_k} = \bar{\mathbf{P}}_{m_k}[1] e^{j \bar{\mathbf{P}}_{m_k}[2]}. \quad (41)$$

Likewise, the additive perturbation vector for $\bar{\mathbf{P}}_{m_k}$ is described by a two-element vector $\bar{\rho}_k = (a_k, \delta_k)$. Similar to (41), we can define another two-element vector, $\bar{\mathbf{P}}_{m_k}$ containing amplitude and phase of the perturbed voltage V_k , such that $\bar{\mathbf{P}}_{m_k} = \bar{\mathbf{P}}_{m_k} + \bar{\rho}_k$. Therefore

$$V_{m_k} = (\bar{\mathbf{P}}_{m_k}[1] + \bar{\rho}_k[1]) e^{j(\bar{\mathbf{P}}_{m_k}[2] + \bar{\rho}_k[2])}. \quad (42)$$

Therefore, the matrix equation in (40) can be rearranged as

$$\dot{\Delta} = \mathbf{M}_{R,m} \Delta \quad (43)$$

where $\Delta = (a_1, \delta_1, a_2, \delta_2, \dots, a_N, \delta_N)^T$ and $\mathbf{M}_{R,m} = \text{circ}(\mathbf{B}_{11}, \mathbf{B}_{12}, \dots, \mathbf{B}_{1N})$. Considering that total admittance matrix of a circularly symmetric oscillator is in circulant form, $\mathbf{M}_{R,m}$ is readily proved to be a block-circulant matrix whose 2×2 block matrices are derived to be

$$\mathbf{B}_{1n} = \begin{bmatrix} \operatorname{Im} \left\{ \frac{\partial \Upsilon_{m_1}}{\partial A_{m_n}} \right\} & \operatorname{Im} \left\{ \frac{\partial \Upsilon_{m_1}}{\partial \theta_{m_n}} \right\} \\ -\operatorname{Re} \left\{ \frac{\partial \Upsilon_{m_1}}{\partial A_{m_n}} \right\} & -\operatorname{Re} \left\{ \frac{\partial \Upsilon_{m_1}}{\partial \theta_{m_n}} \right\} \end{bmatrix}. \quad (44)$$

An oscillation state is stable if real parts of all eigenvalues of its corresponding \mathbf{M}_R are negative. To calculate these eigenvalues, we utilize the linear relationship between the eigenvalues and the matrix elements of a circulant matrix, given by (11), and construct the 2×2 matrix \mathbf{H}_p as

$$\mathbf{H}_p = \sum_{n=1}^N \mathbf{B}_{1n} e^{j(n-1)\frac{2\pi p}{N}} \quad \text{for } p = 0, \dots, N-1. \quad (45)$$

Consequently, the eigenvalues of each \mathbf{H}_p are two eigenvalues of $\mathbf{M}_{R,m}$ [43]. This means that examining the oscillation stability is equivalent to inspecting the eigenvalues of \mathbf{H}_p for $p = 0, \dots, N-1$. \mathbf{H}_p is expanded as (46), as shown at the top of this page, where $\phi_p = 2\pi p/N$. For eigenvalues of \mathbf{H}_p to be negative, $\det(\mathbf{H}_p) > 0$ and $\text{trace}(\mathbf{H}_p) < 0$. In terms of $\Psi_{\bar{A},m}$ and $\Psi_{\bar{\Theta},m}$, it means that

$$\begin{aligned} \operatorname{Im}\{\Psi_{\bar{A},m}(p)\} - \operatorname{Re}\{\Psi_{\bar{\Theta},m}(p)\} &< 0 \\ \operatorname{Im}\{\Psi_{\bar{A},m}^*(p) \times \Psi_{\bar{\Theta},m}(p)\} &> 0 \quad \text{for } p = 0, \dots, N-1. \end{aligned} \quad (47)$$

To examine the stability of an N -port circularly symmetric oscillator, (47) is evaluated. If any of these inequality pairs are not satisfied for a specific p , the mode- p input admittances should be re-designed to resolve the stability issue. This notion will be further clarified in the example in Section V-B.

$$\mathbf{H}_p = \begin{bmatrix} \text{Im} \left\{ \sum_{n=1}^N \frac{\partial \Upsilon_{m_1}}{\partial A_{m_n}} e^{j(n-1)\phi_p} \right\} & \text{Im} \left\{ \sum_{n=1}^N \frac{\partial \Upsilon_{m_1}}{\partial \theta_{m_n}} e^{j(n-1)\phi_p} \right\} \\ -\text{Re} \left\{ \sum_{n=1}^N \frac{\partial \Upsilon_{m_1}}{\partial A_{m_n}} e^{j(n-1)\phi_p} \right\} & -\text{Re} \left\{ \sum_{n=1}^N \frac{\partial \Upsilon_{m_1}}{\partial \theta_{m_n}} e^{j(n-1)\phi_p} \right\} \end{bmatrix} = \begin{bmatrix} \text{Im}\{\Psi_{\bar{A},m}(p)\} & \text{Im}\{\Psi_{\bar{\theta},m}(p)\} \\ -\text{Re}\{\Psi_{\bar{A},m}(p)\} & -\text{Re}\{\Psi_{\bar{\theta},m}(p)\} \end{bmatrix} \quad (46)$$

$$\frac{\partial Y_{t,m_k}}{\partial A_{m_n}} = \begin{cases} -\frac{1}{A_m} \sum_{\substack{l \leq l \leq N \\ l \neq n}} y_{c_{nl}} A_m e^{j(l-n)\phi_m} - \frac{y_{s_{12}} e^{j\phi_m}}{A_m} - \frac{y_{s_{21}} e^{-j\phi_m}}{A_m} \\ + \frac{\partial y_{s_{12}}}{\partial A_{\text{in}}} e^{j\phi_m} + \frac{\partial y_{s_{21}}}{\partial A_{\text{out}}} e^{-j\phi_m} + \frac{\partial y_{s_{11}}}{\partial A_{\text{in}}} + \frac{\partial y_{s_{22}}}{\partial A_{\text{out}}} & \text{for } n = k \\ \frac{y_{c_{12}}}{A_m} e^{j\phi_m} + \frac{y_{s_{12}} e^{j\phi_m}}{A_m} + \frac{\partial y_{s_{12}}}{\partial A_{\text{out}}} e^{j\phi_m} & \text{for } n = k+1 \\ \frac{y_{c_{12}}}{A_m} e^{-j\phi_m} + \frac{y_{s_{21}} e^{-j\phi_m}}{A_m} + \frac{\partial y_{s_{21}}}{\partial A_{\text{in}}} e^{-j\phi_m} & \text{for } n = k-1 \\ \frac{y_{c_{1n}}}{A_m} e^{j(k-n)\phi_m} & \text{Otherwise} \end{cases} \quad (52)$$

B. Stability Analysis of Circular Cavity Oscillator

To study the stability of the circular cavity oscillator in Fig. 8(a), (47) is evaluated. First, we simplify the partial derivatives in (38)

$$\frac{\partial \Upsilon_{m_k}}{\partial A_{m_n}} = \frac{\frac{\partial Y_{t,m_k}}{\partial A_{m_n}}}{\frac{\partial Y_{t,m_k}}{\partial \omega} \Big|_{\omega_{\text{osc}}}} - \frac{Y_{t,m_k}}{\left(\frac{\partial Y_{t,m_k}}{\partial \omega} \Big|_{\omega_{\text{osc}}} \right)^2} \cdot \frac{\partial^2 Y_{t,m_k}}{\partial A_{m_n} \partial \omega} \Big|_{\omega_{\text{osc}}}. \quad (48)$$

The second term in (48) is zero given that $Y_{t,m_k} \Big|_{\omega_{\text{osc}}} = 0$. Similarly, $(\partial \Upsilon_{m_k} / \partial \theta_{m_n})$ can be calculated. As a result, we have

$$\frac{\partial \Upsilon_{m_k}}{\partial A_{m_n}} = \frac{\frac{\partial Y_{t,m_k}}{\partial A_{m_n}}}{\frac{\partial Y_{t,m_k}}{\partial \omega} \Big|_{\omega_{\text{osc}}}}, \quad \frac{\partial \Upsilon_{m_k}}{\partial \theta_{m_n}} = \frac{\frac{\partial Y_{t,m_k}}{\partial \theta_{m_n}}}{\frac{\partial Y_{t,m_k}}{\partial \omega} \Big|_{\omega_{\text{osc}}}}. \quad (49)$$

Assuming that Y_{t,m_k} resembles the behavior of a shunt RLC tank at the vicinity of ω_{osc} , we have

$$\frac{\partial Y_{t,m_k}}{\partial \omega} \Big|_{\omega_{\text{osc}}} = 2jC_{\text{eq}} \quad (50)$$

where C_{eq} denotes the equivalent capacitor of the mode- m input admittance around ω_{osc} . Furthermore, circular symmetry implies that the steady-state solution of (34) is in form of

$$\begin{aligned} A_{m_1} &= A_{m_2} = \cdots = A_{m_N} = A_m \\ \theta_{m_n} &= (n-1)\phi_m \quad \text{for } n = 1, \dots, N. \end{aligned} \quad (51)$$

Therefore, to evaluate (49), $(\partial Y_{t,m_k} / \partial A_{m_n})$ and $(\partial Y_{t,m_k} / \partial \theta_{m_n})$ need to be calculated. From (34)–(36), for $(\partial Y_{t,m_k} / \partial A_{m_n})$, (52), as shown at the top of this page, is concluded, where $(\partial(\cdot) / \partial A_{\text{in}})$ and $(\partial(\cdot) / \partial A_{\text{out}})$ capture the variation of Y-parameters of each ring stage due to small variation of the oscillation amplitude at the input and output of each stage, respectively. This variation itself is a result of nonlinear behavior of the active devices within each stage. Similarly, $(\partial Y_{t,m_k} / \partial \theta_{m_n})$ is found to be

$$\frac{\partial Y_{t,m_k}}{\partial \theta_{m_n}} = \begin{cases} 0 & \text{for } n = k \\ j(y_{c_{12}} + y_{s_{12}}) e^{j\phi_m} & \text{for } n = k+1 \\ j(y_{c_{12}} + y_{s_{21}}) e^{-j\phi_m} & \text{for } n = k-1 \\ jy_{c_{1n}} e^{j(k-n)\phi_m} & \text{Otherwise.} \end{cases} \quad (53)$$

Using (52), $\Psi_{\bar{\theta},m}(p)$ is calculated

$$\begin{aligned} \Psi_{\bar{\theta},m}(p) &= \frac{1}{2jC_{\text{eq}}} \sum_{n=1}^N \frac{\partial Y_{t,m_1}}{\partial \theta_{m_n}} e^{j(n-1)\phi_p} \\ &= \frac{1}{2C_{\text{eq}}} [Y_{c,m+p} + Y_{r,m+p} - (y_{c_{11}} + y_{s_{11}} + y_{s_{22}})] \\ &= \frac{1}{2C_{\text{eq}}} [Y_{t,m+p} - (y_{r_{11}})]. \end{aligned} \quad (54)$$

Similarly, $\Psi_{\bar{A},m}(p)$ is calculated using (52)

$$\begin{aligned} \Psi_{\bar{A},m}(p) &= \frac{1}{2jC_{\text{eq}}} \sum_{n=1}^N \frac{\partial Y_{t,m_1}}{\partial A_n} e^{j(n-1)\phi_p} \\ &= \frac{1}{2jA_m C_{\text{eq}}} [Y_{c,m+p} - Y_{c,m} + Y_{r,m+p} - Y_{r,m}] \\ &\quad + \frac{1}{2jC_{\text{eq}}} \left[\frac{\partial y_{s_{12}}}{\partial A_{\text{out}}} e^{j(\phi_m + \phi_p)} + \frac{\partial y_{s_{21}}}{\partial A_{\text{in}}} e^{-j(\phi_m + \phi_p)} \right. \\ &\quad \left. + \frac{\partial y_{s_{12}}}{\partial A_{\text{in}}} e^{j\phi_m} + \frac{\partial y_{s_{21}}}{\partial A_{\text{out}}} e^{-j\phi_m} + \frac{\partial y_{s_{11}}}{\partial A_{\text{in}}} + \frac{\partial y_{s_{22}}}{\partial A_{\text{out}}} \right] \\ &= \frac{1}{2jC_{\text{eq}}} \left[\frac{(Y_{t,m+p} - Y_{t,m})}{A_m} \right. \\ &\quad \left. + \frac{\partial y_{s_{12}}}{\partial A_{\text{out}}} e^{j(\phi_m + \phi_p)} + \frac{\partial y_{s_{21}}}{\partial A_{\text{in}}} e^{-j(\phi_m + \phi_p)} + \frac{\partial Y_{r_m}}{\partial A} \right] \end{aligned} \quad (55)$$

where $(\partial Y_{r,m} / \partial A)$ denotes the variation of the ring mode- m input admittance due to small variation in the oscillation amplitude. Therefore, by knowing the total input admittance for different modes, as well as the nonlinear characteristics of admittance of each stage of the ring, both $\Psi_{\bar{A},m}(p)$ and $\Psi_{\bar{\theta},m}(p)$ can be evaluated to examine the oscillation stability of the desired oscillation state occurring at 115 GHz in mode-1. Fig. 29 plots the oscillation stability condition in (47) using (54) and (55), indicating a stable oscillation state in this mode.

VI. MEASUREMENT RESULTS

The 114-GHz multi-port circularly polarized radiator is implemented using a 0.13- μm SiGe BiCMOS process. The chip micro-photograph is shown in Fig. 30 with the cavity (1.5 mm diameter) seen at the center of the chip. The core

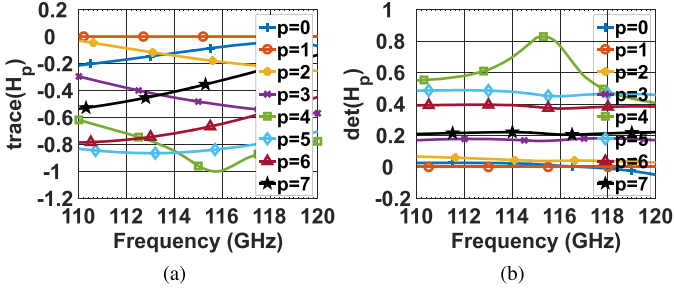


Fig. 29. Simulated oscillation stability conditions for circular cavity oscillator: (a) $\text{trace}(\mathbf{H}_p)$ and (b) $\det(\mathbf{H}_p)$.

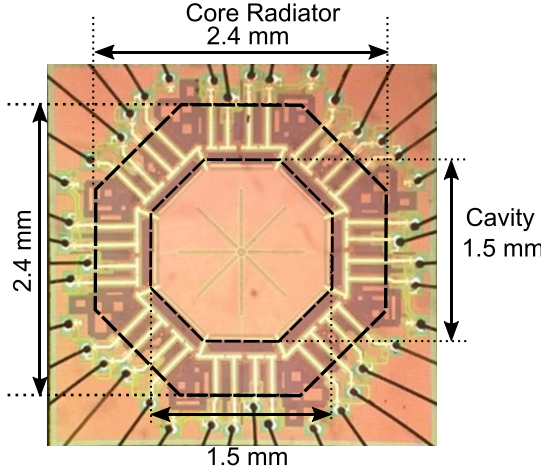


Fig. 30. Chip micro-photograph of the circularly polarized multi-port radiator.

radiator occupies $2.4 \times 2.4 \text{ mm}^2$ of die area and consumes 505 mW of dc power. Also, the eight symmetric radiation slots and the center hole responsible for suppressing the in-phase mode are visible in the die photograph. The dummy metals are placed with higher concentration in less sensitive areas such as those close to the sidewalls and at the center. Minimum amount of dummy metals are placed underneath the radiation slots as it lowers the radiation gain by lowering the field intensity and distorting the field distribution. Finally, the dummy metals are added in a symmetric fashion with respect to the cavity center to avoid any undesired asymmetric perturbation. The ring oscillator is placed on the periphery of the cavity to generate sustainable oscillation and drive the cavity ports in a symmetric fashion. The t-lines within the ring oscillator are implemented using on-chip grounded CPWs with ground plane on metal 1 and the characteristic impedance of 40Ω . Due to the use of grounded sidewalls for the CPWs, stacking of bottom metal layers in order to minimize the return-path loss was found to be unnecessary. The CPW loss optimized in light of the density rules, meaning that the signal linewidth and spacing to ground are chosen, such that no dummy metal filling is required underneath the CPWs, while the density rules are met. Short stubs used within passive networks of the ring, which also provide bias and supply paths to the circuit, are located toward the edges of the chip, where they are connected to bond pads and on-chip decoupling capacitors. Bias, supply, and ground pads are placed symmetrically around the oscillator structure surrounding the cavity to maintain the circular symmetry of the cavity-based radiator. A common mesh ground plane on metal 1 is shared between the bottom

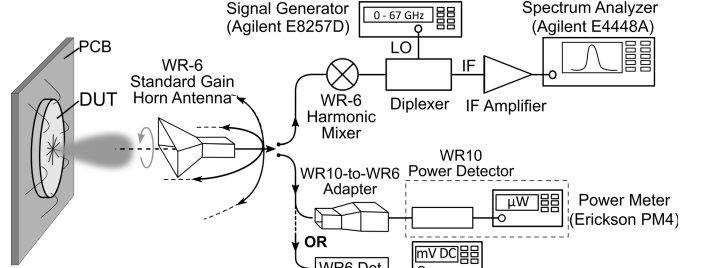


Fig. 31. Measurement setup block diagram.

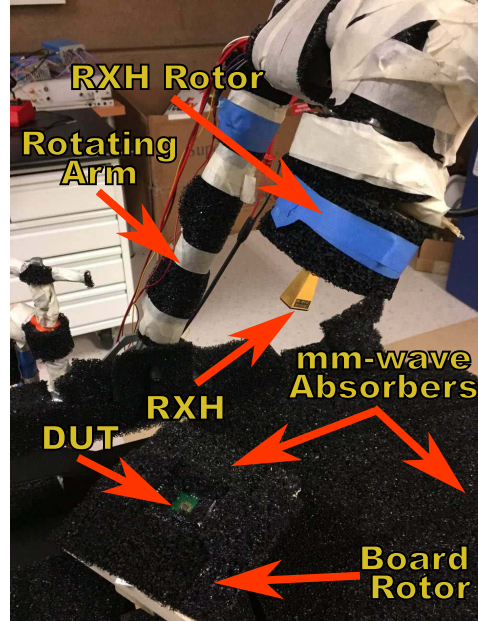


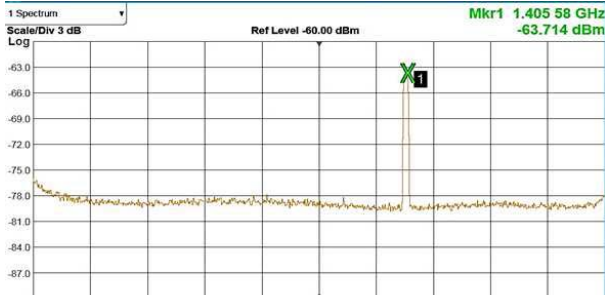
Fig. 32. Photograph of the measurement setup.

plate of the cavity and the ground plane of the CPWs in the ring oscillator. This ground plane is connected to the ground pads on the periphery of the chip.

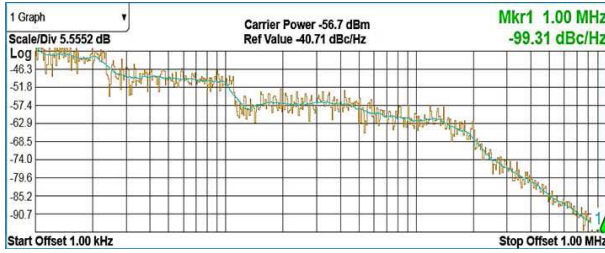
The block diagram of measurement setup is shown in Fig. 31. To bias the chip, it was wire-bonded on a low-cost FR-4 PCB. The radiated signal was captured by a 25-dBi gain linearly polarized WR-6 horn antenna (RXH). For spectrum measurements, the RXH output was down-converted to the IF domain at a frequency of $f_{\text{IF}} \approx 1.4 \text{ GHz}$ using a WR6 10-th harmonic mixer followed by a low-noise IF amplifier. Harmonic number of the mixer, N , was verified by changing the local oscillator frequency, f_{LO} , and monitoring the shift in the IF frequency, f_{IF} as $\Delta f_{\text{IF}} = N \times \Delta f_{\text{LO}}$.

The measurement setup in Fig. 32 shows the radiator chip and the RXH mounted on a rotating arm. Both the RXH and the PCB board are also mounted to stepper motors, enabling measurement at an arbitrary angle with three degrees of freedom. Several ECCOSORB-HR absorbers were placed around the chip to minimize multipath reflections. The absorbers have been verified to show at least 15-dB attenuation at this frequency.

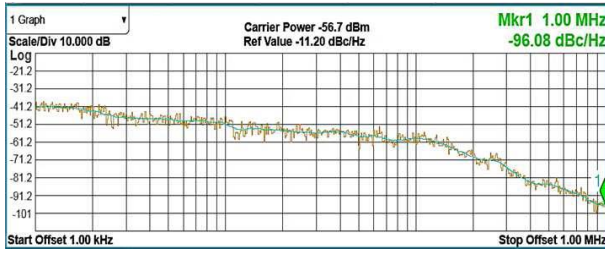
Fig. 34(a) shows the spectrum of the down-converted signal, measured by E4148 Keysight Signal Analyzer, indicating an RF frequency of 114.1 GHz for the radiated signal. The phase noise of the radiated signal was also characterized by measuring the phase noise of the IF signal. The measured phase



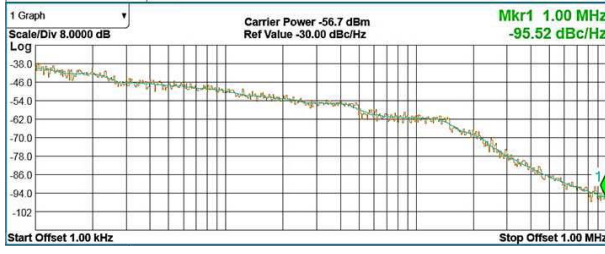
(a)



(b)



(c)

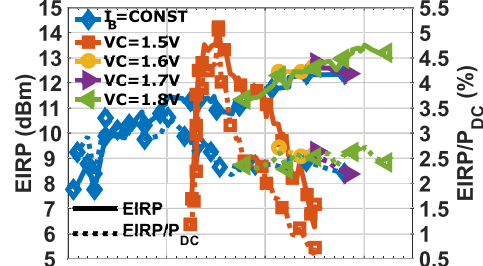


(d)

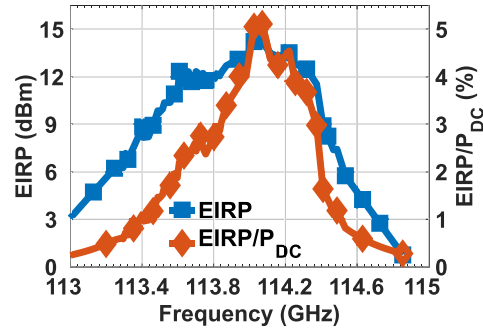
Fig. 33. (a) Measured spectrum of down-converted radiator output indicating radiation at 114.1 GHz. (b) Measurement phase noise of the down-converted radiated signal. (c) and (d) Average and worst phase-noise profiles.

noise profile of the radiator is shown in Fig. 34(b), indicating a phase noise of -99.3 dBc/Hz at 1-MHz offset. To verify the frequency stability of the radiator, the spectrum and the phase noise were measured for three radiator samples under different bias settings. Fig. 34(c) and (d) shows the average and worst phase noise profiles of these three prototypes, retrospectively, all indicating a phase noise better than -95.5 dBc/Hz at 1-MHz offset. The average phase noise of these 20 samples was better than -96 dBc/Hz at 1-MHz offset. The low-phase-noise operation is achieved owing to high Q of the cavity resonance and noise reduction due to coupling of the ring ports through the cavity.

For EIRP measurements, the RXH was followed by a PM4 Erikson power meter. The aperture size D of the RXH used in the measurement was 1.6 mm. Therefore, the minimum



(a)



(b)

Fig. 34. (a) Measured EIRP and dc-to-EIRP conversion efficiency versus radiator dc power consumption. (b) Measured EIRP and dc-to-EIRP conversion efficiency versus frequency.

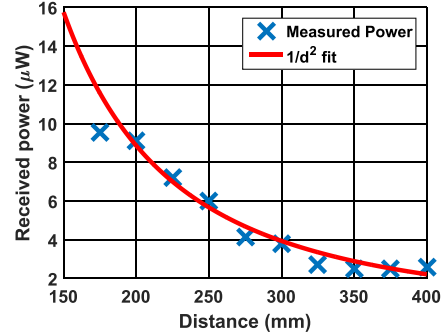


Fig. 35. Received power versus distance.

far-field distance ($= 2D^2/\lambda$) is 19.5 cm. The EIRP was measured at 20 cm of distance with a peak value of 14.2 dBm, while the chip dc power consumption (P_{dc}) was 505 mW, leading to 5.2% dc-to-EIRP conversion efficiency without using silicon lens. Using this measurement, the spectrum test setup was calibrated [19].

Next, the bias current and the supply voltage of the oscillator were varied to characterize its impact on the oscillation power and frequency. Fig. 35(a) shows the measured EIRP and dc-to-EIRP conversion efficiency versus chip dc power consumption for different bias settings. It is seen that EIRP remains above 6 dBm, while the chip power consumption varies by more than 100% (0.2–0.86 W). Monitoring the spectrum shown in Fig. 35(b) also reveals that the oscillation frequency variation is only 1.3 GHz (113.2–114.5 GHz) under this bias and supply variation, which is less than 1% of the center frequency. Robustness of the oscillation is thus concluded from these experiments. Such frequency robustness is achieved primarily because of the high Q and sharp resonance of the cavity.

TABLE I
TABLE OF PERFORMANCE COMPARISON, COMPARING THIS PAPER WITH ALL RECENTLY PUBLISHED
PRIOR WORK NOT USING SILICON LENS OR ANY POSTPROCESSING

REF	This work	[14]	[19]	[21]	[20]	[3]	[26]
Polarization	Circular	Linear/ Circular/ Elliptic	Circular	Linear/ Circular/ Elliptic	Circular	Linear	Linear
Freq. (GHz)	114	122.9	134.5	105.5	161	210	338
EIRP (dBm)	14.2	12.3	6	7.8	4.6	5.13	17.1
EIRP-per-element (dBm)	14.2	6.3	6	4.8	4.6	-0.87	5.1
Total Radiated Power (dBm)	8.2	0.05	-1.3	-0.5	-2	-5.5	-0.9
P.N. (dBc/Hz) [*]	-99.3	NA	NA	NA	NA	-81**	-93
P _{DC} (mW)	505	1885	168	476	388	240	1540
EIRP/P _{DC} (%)	5.2	0.9	2.37	1.26	0.74	1.4	3.33
DC-to-Radiation Efficiency (%)	1.31	0.05	0.44	0.19	0.16	0.11	0.05
Area (mm ²)	5.76	8.12	1.2	2.64	1	3.5	3.9
Radiated Power/Area (mW/mm ²)	1.15	0.12	0.62	0.34	0.63	0.08	0.21
f _{max} (GHz)	260	320	320	320	300	320	260
Tech.	0.13µm SiGe BiCMOS	32nm CMOS SOI	32nm CMOS SOI	32nm CMOS SOI	0.13µm SiGe BiCMOS	32nm CMOS SOI	65nm CMOS Bulk

* Phase-noise at 1MHz offset

** Measured phase noise reported for VCO break-out

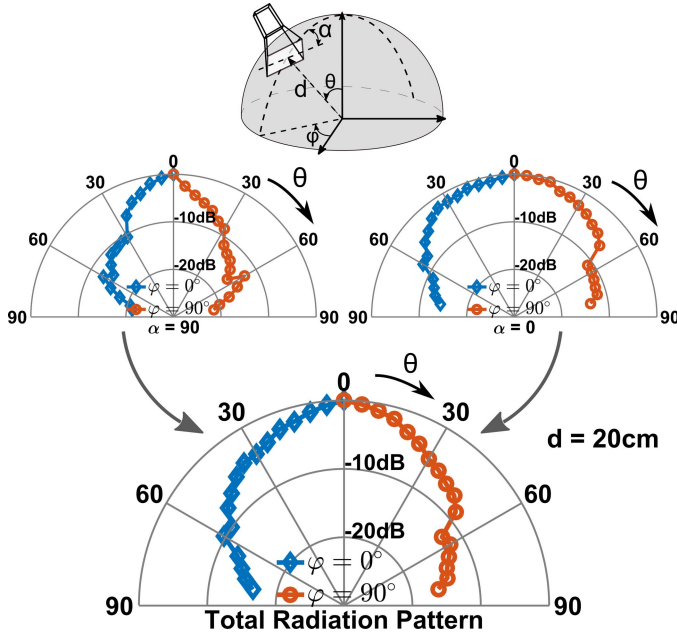


Fig. 36. Radiation pattern: procedure and measurement results.

Fig. 35 shows the received power versus distance between the radiator chip and the RXH. This received power plot follows the profile predicted by the Friis equation, verifying the reception in the far field.

To characterize the radiation pattern, the received power was captured using a WR6 power detector, while RXH was swept along the θ direction in two orthogonal azimuthal planes of $\varphi = 0^\circ$ and $\varphi = 90^\circ$. Owing to the fact that only the normalized received power at different directions is of interest in this measurement, the small size and the low weight of the power detector compared the PM4 power meter help the mechanical rigidity of the RX antenna fixture and, thus, accuracy of the measurements. Since RXH polarization was linear whereas that of the radiated signal was of circular, the received power

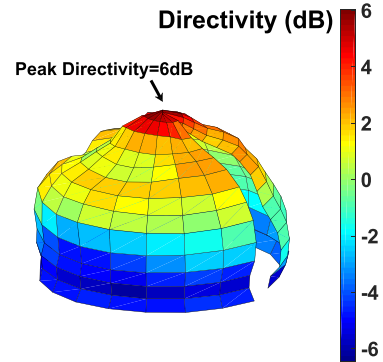


Fig. 37. Measured 3-D radiation pattern.

in each plane was recorded for two orthogonal directions, namely, two angles of $\alpha = 0^\circ$ and $\alpha = 90^\circ$ between RXH and the sweep path, thereby completely capturing the received power (Fig. 36) [19]. The measured radiation patterns indicate a symmetric pattern with respect to boresight ($\theta = 0^\circ$), which is consistent with our expectation from this rotationally symmetric radiator. The total radiation pattern can then be calculated using the vector summation of the measurements for $\alpha = 0^\circ$ and $\alpha = 90^\circ$. The resultant pattern is shown in Fig. 36.

As for the measurement of the total radiated power, output of the power detector was calibrated using the PM4 power meter. Then, the received power was captured at different angles using the power detector. The total radiated power was then calculated by integrating the received power density over the entire measurement surface. Fig. 37 demonstrates the measured 3-D radiation pattern. The measured directivity and the output power are 6 dBi and 8.2 dBm, respectively, leading to the measured dc-to-radiation efficiency of 1.3%.²

The polarization pattern at the boresight direction was measured by sweeping α from 0° to 360° . Variation of the

²The output power reported in [44] is the total oscillation power injected to the cavity, which was obtained by de-embedding the simulated antenna gain from the measured EIRP.

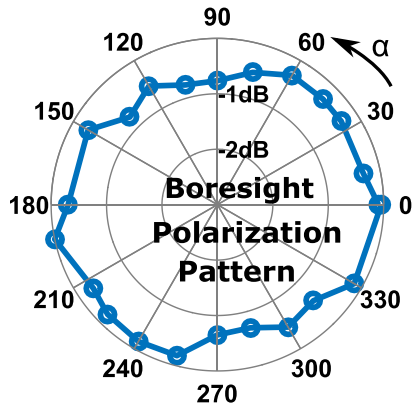


Fig. 38. Measured polarization pattern.

received power was less than 0.8 dB indicating an axial ratio of 0.8 dB, as shown in Fig. 38.

Table I provides the performance summary of this radiator in comparison with the state of the art. This paper demonstrates a fundamental-frequency circularly polarized radiator with the highest radiated power, dc-to-radiation efficiency, dc-to-EIRP conversion efficiency, and lowest phase noise among silicon radiators without using silicon lens or any external locking signal.

VII. CONCLUSION

A multi-port fundamental-frequency oscillator/radiator structure incorporating a multi-port circular-cavity-backed antenna as a monolithic resonator, power combiner, and radiator was introduced. It was shown that the rotationally symmetric multi-port structure facilitates generation and constructive power combining of distinct evenly spaced oscillation phases which, in turn, enable circularly polarized radiation. A general theory of multi-port oscillators—and in particular, the widely used circularly symmetric oscillator topologies—was presented. Using the results of this analysis, the oscillator design procedure was performed in light of extracting maximum power from transistors by providing optimum voltage-gain condition. As a result, high output power and high dc-to-EIRP conversion efficiency for the desired mode of oscillation state was achieved, while all other modes were suppressed. Fabricated in a $0.13\text{-}\mu\text{m}$ SiGe BiCMOS process, the prototype chip has achieved 14.2-dBm EIRP and 8.2-dBm radiated power at 114.1 GHz translating to 5.2% dc-to-EIRP conversion efficiency and 1.3% dc-to-radiation efficiency, respectively, without using silicon lens or any external locking signal. The radiated signal exhibited -99.3 dBc/Hz phase noise at 1-MHz offset.

ACKNOWLEDGMENT

The authors would like to thank Towerjazz Semiconductor for chip fabrication, and D. Huh and N. Shafiq from Keysight Technologies and Prof. G. Rebeiz from UCSD for providing measurement equipment.

REFERENCES

- [1] N. Dolatsha *et al.*, “A compact 130 GHz fully packaged point-to-point wireless system with 3D-printed 26 dBi lens antenna achieving 12.5 Gb/s at 1.55 pJ/b/m,” in *IEEE Int. Solid-State Circuits Conf. (ISSCC) Dig. Tech. Papers*, Feb. 2017, pp. 306–307.
- [2] K. Katayama *et al.*, “A 300 GHz CMOS transmitter with 32-QAM 17.5 Gb/s/ch capability over six channels,” *IEEE J. Solid-State Circuits*, vol. 51, no. 12, pp. 3037–3048, Dec. 2016.
- [3] Z. Wang, P.-Y. Chiang, P. Nazari, C.-C. Wang, Z. Chen, and P. Heydari, “A CMOS 210-GHz fundamental transceiver with OOK modulation,” *IEEE J. Solid-State Circuits*, vol. 49, no. 3, pp. 564–580, Mar. 2014.
- [4] F. Caster, L. Gilreath, S. Pan, Z. Wang, F. Capolino, and P. Heydari, “Design and analysis of a W-band 9-element imaging array receiver using spatial-overlapping super-pixels in silicon,” *IEEE J. Solid-State Circuits*, vol. 49, no. 6, pp. 1317–1332, Jun. 2014.
- [5] R. Han *et al.*, “A 320 GHz phase-locked transmitter with 3.3 mW radiated power and 22.5 dBm EIRP for heterodyne THz imaging systems,” in *IEEE Int. Solid-State Circuits Conf. (ISSCC) Dig. Tech. Papers*, Feb. 2015, pp. 1–3.
- [6] S. P. Voinigescu, S. Shopov, J. Bateman, H. Farooq, J. Hoffman, and K. Vasilakopoulos, “Silicon millimeter-wave, terahertz, and high-speed fiber-optic device and benchmark circuit scaling through the 2030 ITRS horizon,” *Proc. IEEE*, vol. 105, no. 6, pp. 1087–1104, Jun. 2017.
- [7] R. Han and E. Afshari, “A CMOS high-power broadband 260-GHz radiator array for spectroscopy,” *IEEE J. Solid-State Circuits*, vol. 48, no. 12, pp. 3090–3104, Dec. 2013.
- [8] O. Momeni and E. Afshari, “High power terahertz and millimeter-wave oscillator design: A systematic approach,” *IEEE J. Solid-State Circuits*, vol. 46, no. 3, pp. 583–597, Mar. 2011.
- [9] M. Adnan and E. Afshari, “A 247-to-263.5 GHz VCO with 2.6 mW peak output power and 1.14% DC-to-RF efficiency in 65 nm bulk CMOS,” in *IEEE Int. Solid-State Circuits Conf. (ISSCC) Dig. Tech. Papers*, Feb. 2014, pp. 262–263.
- [10] P.-Y. Chiang, Z. Wang, O. Momeni, and P. Heydari, “A 300 GHz frequency synthesizer with 7.9% locking range in 90 nm SiGe BiCMOS,” in *IEEE Int. Solid-State Circuits Conf. (ISSCC) Dig. Tech. Papers*, Feb. 2014, pp. 260–261.
- [11] Y. M. Tousi, O. Momeni, and E. Afshari, “A 283-to-296 GHz VCO with 0.76 mW peak output power in 65 nm CMOS,” in *IEEE Int. Solid-State Circuits Conf. (ISSCC) Dig. Tech. Papers*, Feb. 2012, pp. 258–259.
- [12] C. Jiang *et al.*, “A fully integrated 320 GHz coherent imaging transceiver in 130 nm SiGe BiCMOS,” *IEEE J. Solid-State Circuits*, vol. 51, no. 11, pp. 2596–2609, Nov. 2016.
- [13] Y. Shang, H. Yu, H. Fu, and W. M. Lim, “A 239–281 GHz CMOS receiver with on-chip circular-polarized substrate integrated waveguide antenna for sub-terahertz imaging,” *IEEE Trans. THz Sci. Technol.*, vol. 4, no. 6, pp. 686–695, Nov. 2014.
- [14] A. Safarpour, S. M. Bowers, K. Dasgupta, and A. Hajimiri, “Dynamic polarization control of two-dimensional integrated phased arrays,” *IEEE Trans. Microw. Theory Techn.*, vol. 64, no. 4, pp. 1066–1077, Apr. 2016.
- [15] K. Sengupta and A. Hajimiri, “Distributed active radiation for THz signal generation,” in *IEEE Int. Solid-State Circuits Conf. (ISSCC) Dig. Tech. Papers*, Feb. 2011, pp. 288–289.
- [16] K. Sengupta and A. Hajimiri, “Sub-THz beam-forming using near-field coupling of distributed active radiator arrays,” in *Proc. IEEE Radio Freq. Integr. Circuits Symp.*, Jun. 2011, pp. 1–4.
- [17] K. Sengupta and A. Hajimiri, “A 0.28 THz power-generation and beam-steering array in CMOS based on distributed active radiators,” *IEEE J. Solid-State Circuits*, vol. 47, no. 12, pp. 3013–3031, Dec. 2012.
- [18] K. Sengupta and A. Hajimiri, “Mutual synchronization for power generation and beam-steering in CMOS with on-chip sense antennas near 200 GHz,” *IEEE Trans. Microw. Theory Techn.*, vol. 63, no. 9, pp. 2867–2876, Sep. 2015.
- [19] S. M. Bowers, A. Safarpour, and A. Hajimiri, “An integrated slot-ring traveling-wave radiator,” *IEEE Trans. Microw. Theory Techn.*, vol. 63, no. 4, pp. 1154–1162, Apr. 2015.
- [20] S. M. Bowers and A. Hajimiri, “Multi-port driven radiators,” *IEEE Trans. Microw. Theory Techn.*, vol. 61, no. 12, pp. 4428–4441, Dec. 2013.
- [21] S. M. Bowers, A. Safarpour, and A. Hajimiri, “Dynamic polarization control,” *IEEE J. Solid-State Circuits*, vol. 50, no. 5, pp. 1224–1236, May 2015.
- [22] M. F. Karim *et al.*, “Integration of SiP-based 60-GHz 4×4 antenna array with CMOS OOK transmitter and LNA,” *IEEE Trans. Microw. Theory Techn.*, vol. 59, no. 7, pp. 1869–1878, Jul. 2011.
- [23] C. A. Balanis, *Antenna Theory and Design*. New York, NY, USA: Wiley, 2016.
- [24] Z. Wang and P. Heydari, “A study of operating condition and design methods to achieve the upper limit of power gain in amplifiers at near- f_{max} frequencies,” *IEEE Trans. Circuits Syst. I, Reg. Papers*, vol. 64, no. 2, pp. 261–271, Feb. 2017.

- [25] O. Momeni and E. Afshari, "A high gain 107 GHz amplifier in 130 nm CMOS," in *Proc. IEEE Custom Integr. Circuits Conf. (CICC)*, Sep. 2011, pp. 1–4.
- [26] Y. Tousi and E. Afshari, "A scalable THz 2D phased array with +17 dBm of EIRP at 338 GHz in 65 nm bulk CMOS," in *IEEE Int. Solid-State Circuits Conf. (ISSCC) Dig. Tech. Papers*, Feb. 2014, pp. 258–259.
- [27] A. Safarpour, S. M. Bowers, K. Dasgupta, and A. Hajimiri, "A 2×2 dynamic polarization-controlling integrated phased array," in *Proc. IEEE Radio Freq. Integr. Circuits Symp. (RFIC)*, May 2015, pp. 219–222.
- [28] K. Kurokawa, "The single-cavity multiple-device oscillator," *IEEE Trans. Microw. Theory Techn.*, vol. MTT-19, no. 10, pp. 793–801, Oct. 1971.
- [29] A. Mirzaei, M. E. Heidari, R. Bagheri, S. Chehrazi, and A. A. Abidi, "The quadrature LC oscillator: A complete portrait based on injection locking," *IEEE J. Solid-State Circuits*, vol. 42, no. 9, pp. 1916–1932, Sep. 2007.
- [30] E. Laskin, P. Chevalier, A. Chantre, B. Sautreuil, and S. P. Voinigescu, "165-GHz transceiver in SiGe technology," *IEEE J. Solid-State Circuits*, vol. 43, no. 5, pp. 1087–1100, May 2008.
- [31] K. Kurokawa, "Injection locking of microwave solid-state oscillators," *Proc. IEEE*, vol. 61, no. 10, pp. 1386–1410, Oct. 1973.
- [32] R. A. York, P. Liao, and J. J. Lynch, "Oscillator array dynamics with broadband N -port coupling networks," *IEEE Trans. Microw. Theory Techn.*, vol. 42, no. 11, pp. 2040–2045, Nov. 1994.
- [33] K. Kurokawa, "Some basic characteristics of broadband negative resistance oscillator circuits," *Bell Syst. Tech. J.*, vol. 48, no. 6, pp. 1937–1955, Jul. 1969.
- [34] C. T. Rucker, "A multiple-diode high-average-power avalanche-diode oscillator (correspondence)," *IEEE Trans. Microw. Theory Techn.*, vol. MTT-17, no. 12, pp. 1156–1158, Dec. 1969.
- [35] K. Kurokawa, "An analysis of Rucker's multidevice symmetrical oscillator (correspondence)," *IEEE Trans. Microw. Theory Techn.*, vol. MTT-18, no. 11, pp. 967–969, Nov. 1970.
- [36] D. Pozar, *Microwave Engineering*. New York, NY, USA: Wiley, 2011.
- [37] M. S. Mahani and G. W. Roberts, "A mmWave folded substrate integrated waveguide in a 130-nm CMOS process," *IEEE Trans. Microw. Theory Techn.*, vol. 65, no. 8, pp. 2775–2788, Aug. 2017.
- [38] S. Hu *et al.*, "A SiGe BiCMOS transmitter/receiver chipset with on-chip SIW antennas for terahertz applications," *IEEE J. Solid-State Circuits*, vol. 47, no. 11, pp. 2654–2664, Nov. 2012.
- [39] H. J. Tang, G. Q. Yang, J. X. Chen, W. Hong, and K. Wu, "Millimeter-wave and terahertz transmission loss of CMOS process-based substrate integrated waveguide," in *IEEE MTT-S Int. Microw. Symp. Dig.*, Jun. 2012, pp. 1–3.
- [40] Z. Wang, P. Nazari, and P. Heydari, "Bottom-feed on-chip waveguide slot antenna for THz applications," in *Proc. IEEE Int. Symp. Antennas Propag., USNC/URSI Nat. Radio Sci. Meet.*, Jul. 2015, pp. 1458–1459.
- [41] D. Yuanzhu, "Circular polarization slot antenna apparatus capable of being easily miniaturized," U.S. Patent 2005 0,104,793 A1, May 19, 2005. [Online]. Available: <http://www.google.com/patents/US20050104793>
- [42] O. Momeni, "A 260 GHz amplifier with 9.2 dB gain and –3.9 dBm saturated power in 65 nm CMOS," in *IEEE Int. Solid-State Circuits Conf. (ISSCC) Dig. Tech. Papers*, Feb. 2013, pp. 140–141.
- [43] G. J. Tee, "Eigenvectors of block circulant and alternating circulant matrices," *New Zealand J. Math.*, vol. 36, pp. 195–211, 2007.
- [44] P. Nazari, S. Jafarlou, and P. Heydari, "A fundamental-frequency 114 GHz circular-polarized radiating element with 14 dBm EIRP, –99.3 dBc/Hz phase-noise at 1 MHz offset and 3.7% peak efficiency," in *IEEE Int. Solid-State Circuits Conf. (ISSCC) Dig. Tech. Papers*, Feb. 2017, pp. 322–323.



Peyman Nazari (S'10) received the B.S degree in electrical engineering from the Sharif University of Technology, Tehran, Iran, in 2010, and the M.Sc. and Ph.D. degrees in electrical engineering from the University of California at Irvine (UCI), Irvine, CA, USA, in 2015 and 2017, respectively.

He joined the Nanoscale Communication IC Labs, UCI, where he was involved in sub-THz RF transceiver and radiator design in CMOS and BiCMOS technology. From 2012 to 2013, he was with Qualcomm Inc., San Diego, CA, USA, where he was involved in the design on power amplifiers and power detectors in advanced CMOS technology and has been involved in millimeter-wave (mm-wave) 5G radios since 2017. His current research interests include analog/RF/mm-wave circuit design, mm-wave and sub-THz signal generation, power amplification, and receiver design in silicon technologies.



Saman Jafarlou (S'10) received the B.Sc. degree in electrical and computer engineering from the University of Tehran, Tehran, Iran, in 2010, and the M.Sc. degree in electrical and computer engineering from the University of Waterloo, Waterloo, ON, Canada, in 2012. He is currently pursuing the Ph.D. degree in electrical engineering and computer science with the University of California at Irvine, Irvine, CA, USA.

He was with Peraso Tech. Inc., Toronto, ON, Canada, in 2013, where he was involved in developing 60-GHz wireless chip sets. From 2016 to 2017, he was with Qualcomm Inc., Irvine, CA, and Apple Inc., Cupertino, CA, USA, where he was involved in the design of CMOS power amplifiers and signal/power integrity of RF systems. His current research interests include RF, millimeter-wave/THz integrated circuits design for wireless communication systems, and imaging applications.



Payam Heydari (M'01–SM'09–F'17) received the B.S. and M.S. degrees (Hons.) in electrical engineering from the Sharif University of Technology, Tehran, Iran, in 1992 and 1995, respectively, and the Ph.D. degree from the University of Southern California in 2001.

His group was among the first groups who introduced the design of millimeter-wave (mm-wave) integrated circuits in silicon process. They demonstrated the world's first fundamental frequency CMOS transceiver operating above 200 GHz and the world's highest frequency synthesizer in silicon at 300 GHz. He is currently a Full Professor of electrical engineering with the University of California at Irvine (UCI), Irvine, CA, USA. He is also the Director of the Nanoscale Communication IC Labs. He is the co-author of two books, one book chapter, and more than 130 journal and conference papers. His current research interests include the design of terahertz/mm-wave/RF and analog integrated circuits.

Dr. Heydari was a Distinguished Lecturer of the IEEE Solid-State Circuits Society from 2014 to 2016. He was a recipient of the Best Paper Award at the 2000 IEEE International Conference on Computer Design, the 2001 Technical Excellence Award from the Association of Professors and Scholars of Iranian Heritage, the 2005 IEEE Circuits and Systems Society Darlington Award, the 2005 National Science Foundation CAREER Award, the 2005 Henry Samueli School of Engineering Teaching Excellence Award, the 2007 IEEE Circuits and Systems Society Guillemin-Cauer Award, the 2009 School of Engineering Best Faculty Research Award, the 2009 Business Plan Competition First Place Prize Award and the Best Concept Paper Award from the Paul Merage School of Business at UCI, the 2010 Faculty of the Year Award from UCI's Engineering Student Council, the 2014 Distinguished Engineering Educator Award from Orange County Engineering Council, and the 2016–2017 UCI's School of Engineering Mid-Career Excellence in Research. He was recognized as the 2004 Outstanding Faculty at the Electrical Engineering and Computer Science Department, UCI. His research on novel low-power multi-purpose multi-antenna RF front ends received the Low-Power Design Contest Award at the 2008 IEEE International Symposium on Low-Power Electronics and Design (ISLPED). He was named as one of ten outstanding innovators by the Office of Technology Alliances at UCI. He has given the keynote speech to the IEEE GlobalSIP 2013 Symposium on Millimeter Wave Imaging and Communications. He served as an Invited Distinguished Speaker to the 2014 IEEE Midwest Symposium on Circuits and Systems, and gave a tutorial at the 2017 International Solid-State Circuits Conference (ISSCC).

He served on the technical program committees of the Compound Semiconductor IC Symposium, the Custom Integrated Circuits Conference, and ISLPED. He served on the technical program committees of the International Symposium on Quality Electronic Design, the IEEE Design and Test in Europe, and the International Symposium on Physical Design. He currently serves on the Technical Program Committee of ISSCC. He served as the Guest Editor of the IEEE JOURNAL OF SOLID-STATE CIRCUITS and an Associate Editor of the IEEE TRANSACTIONS ON CIRCUITS AND SYSTEMS—I.